

# Discovery and analysis of low surface brightness galaxies in the environment of NGC 1052

Javier Román<sup>1,2,3★</sup>, Aida Castilla<sup>4</sup>, and Javier Pascual-Granado<sup>1</sup>

<sup>1</sup> Instituto de Astrofísica de Andalucía (CSIC), Glorieta de la Astronomía, 18008 Granada, Spain

<sup>2</sup> Instituto de Astrofísica de Canarias, c/ Vía Láctea s/n, E-38205, La Laguna, Tenerife, Spain

<sup>3</sup> Departamento de Astrofísica, Universidad de La Laguna, E-38206, La Laguna, Tenerife, Spain

<sup>4</sup> Universidad Internacional de Valencia (VIU), Pintor Sorolla 21, 46002 Valencia (Spain)

May 24, 2022

## ABSTRACT

The environment of NGC 1052 has recently attracted much attention due to the presence of low surface brightness galaxies (LSBGs) with claimed exotic properties, making the detection of new objects in this region of high interest. We have used public deep photometric data from the Dark Energy Camera Legacy Survey to carry out a comprehensive search for LSBGs over a wide region of  $6 \times 6$  degrees, equivalent to  $2 \times 2$  Mpc at the distance of NGC 1052. We detected 42 LSBGs with  $r_{\text{eff}} > 5$  arcsec and  $\mu_g(0) > 24$  mag arcsec<sup>-2</sup>, of which 20 are previously undetected objects. Among all the newly detected objects, RCP 32 stands out with extreme properties:  $r_{\text{eff}} = 23.0$  arcsec and  $\langle \mu_g \rangle_{\text{eff}} = 28.6$  mag arcsec<sup>-2</sup>. This makes RCP 32 one of the lowest surface brightness galaxies ever detected through integrated photometry, located at just 10 arcmin from the extensively studied NGC 1052-DF2. We explored the presence of globular clusters (GCs) in the LSBGs. We marginally detected a GC system in RCP 32, and argue the great interest of follow-up observations on RCP 32 given its extremely low baryon density. After analyzing the distribution of galaxies with available spectroscopy, we identified a large-scale structure of approximately 1 Mpc, well isolated in redshift-space, centred on NGC 1052. The spatial correlation analysis between the LSBGs and this large-scale structure suggests their association. However, when exploring the distribution of effective radius we found an overpopulation of large LSBGs ( $r_{\text{eff}} > 15$  arcsec) located close to the line of sight of NGC 1052. We argue that this is suggestive of a substructure with similar radial velocity in sight projection, but at a closer distance, to which some of these apparently larger LSBGs could be associated, however possible effects derived from tidal interactions are worth further study. Our work expands the catalogue of LSBGs with new interesting objects and provides a detailed environmental context for the study of LSBGs in this region.

**Key words.** Galaxies: dwarf – Galaxies: photometry – Galaxies: groups

## 1. Introduction

Low surface brightness galaxies (LSBGs) are the dominant population of the faint end of the galaxy luminosity function (e.g., Blanton et al. 2005; Geller et al. 2012; Martin et al. 2019). Due to their low baryon density, LSBGs are an excellent laboratory for testing galactic formation and evolution models (Bothun et al. 1987; Kennicutt 1989; Bullock et al. 2001; de Blok et al. 2001; Sales et al. 2020) and provide important observational constraints on the  $\Lambda$ -CDM cosmological paradigm (e.g., Moore et al. 1999; Klypin et al. 1999; Bullock & Boylan-Kolchin 2017). Traditionally defined as those galaxies fainter than the surface brightness of the night sky,  $\mu_V > 22$  mag arcsec<sup>-2</sup> (Sandage & Binggeli 1984; Impey et al. 1988; Ferguson & Sandage 1988; Bothun et al. 1991; Dalcanton et al. 1997), LSBGs are broadly defined currently as those galaxies fainter than the surface brightness detection limit of the Sloan Digital Sky Survey for small apparent size objects, that is approximately 24 mag arcsec<sup>-2</sup> in the  $g$  band.

Due to their inherent low surface brightness, the detection of new LSBGs is severely limited by depth and data processing, where correct flat-fielding and sky subtraction are crucial steps. Continuous advances in the design and construction of deep multi-purpose optical surveys such as the IAC Stripe82

Legacy Survey (Abazajian et al. 2009; Fliri & Trujillo 2016; Román & Trujillo 2018), the Dark Energy Camera Legacy Survey (DECaLS; Dark Energy Survey Collaboration et al. 2016), the Hyper Suprime-Cam Subaru Strategic Program (HSC-SSP Aihara et al. 2018) and more, are promoting active research in the field of LSBGs (e.g., van Dokkum et al. 2015; Koda et al. 2015; Román & Trujillo 2017b; Venhola et al. 2017; Greco et al. 2018; Prole et al. 2019a; Tanoglidis et al. 2021) and the number of new detected LSBGs is increasing dramatically. However, the possibility of accessing data with lower surface brightness limits is not enough to obtain an unbiased view of this low-mass and low-brightness galactic population, and numerous challenges are still present in their study. For instance, traditional computational utilities for automated source detection/analysis are usually not efficient for low surface brightness objects. This implies the need for specialized software to perform detection and photometry that maximizes the potential provided by the data (see a review by Haigh et al. 2021). Another aspect is related to automatic morphological classification and the identification of artifacts that parametrically mimic LSBGs, such as reflections, faint clumped sources or inaccurate deblending identifications. Human visual inspection is capable of removing the vast majority of these false positives with high efficiency, but for large data sets this is a very tedious and even unaffordable task. While the use of deep learning procedures has recently proven efficient in

★ e-mail: jromanastro@gmail.com

the identification of false positives (e.g., Tuccillo et al. 2018; Burke et al. 2019; Tanoglidis et al. 2021) with an accuracy of around 90%, the accuracy of human visual identification has not yet been reached.

Obtaining radial velocities through optical spectroscopy for complete samples of LSBGs is prohibitive in terms of observational time, and objects not resolved into stars (thus outside the scope of star-counting techniques), without the presence of HI gas and with extremely low surface brightness ( $\mu > 26$  mag arcsec<sup>-2</sup>) are particularly problematic. This has restored importance to traditionally secondary methods in estimating distances, such as the surface brightness fluctuation method (e.g., Carlsten et al. 2019; Greco et al. 2021; Zonoozi et al. 2021) or the use of the peak of the globular cluster luminosity function as a standard candle (e.g., Román et al. 2019).

With the increasing depth of available photometric data, and therefore the diminishing surface brightness of the detected objects, the study of LSBGs is thus more and more challenging. A need exists to develop increasingly advanced analysis techniques in the face of the imminent arrival of the new generation of deep optical and infrared surveys such as the Legacy Survey of Space and Time (LSST; LSST Science Collaboration et al. 2009), Euclid (Laureijs et al. 2011) or the Nancy Grace Roman Space Telescope (Spergel et al. 2015), among many others.

In this work we aim to explore the presence and properties of LSBGs in the environment of the NGC 1052 group of galaxies. This region is of particular interest due to the exotic properties that recent works claim for some LSBGs found in this region. For instance, van Dokkum et al. (2018a) in [KKS2000] 04 (more commonly known as NGC 1052-DF2) and van Dokkum et al. (2019a) in NGC 1052-DF4 claimed the similarity between the observed baryonic matter and the dynamic matter obtained by the radial velocity dispersion of their globular clusters and also the stellar component (Emsellem et al. 2019; Danieli et al. 2019). This observational evidence would imply an extreme and unexpected deficit (even lack) of dark matter in these LSBGs. Taking into account that their metallicity content follows the usual stellar mass vs. metallicity relation for dwarf galaxies (Fensch et al. 2019; Ruiz-Lara et al. 2019), the possibility that they are tidal dwarf galaxies – galaxies formed by strong interactions with recycled material from massive host galaxies, high in metals, and intrinsically born with a lack of dark matter (see e.g., Duc 2012; Román et al. 2021) – is ruled out. The properties of these LSBGs have been the subject of much debate (see e.g., Martin et al. 2018; Ogiya 2018; Famaey et al. 2018; Kroupa et al. 2018; Lewis et al. 2020; Haslbauer et al. 2019; Müller et al. 2019; Nusser 2019; Montes et al. 2020, 2021). One hypothesis put forward by Trujillo et al. (2019) is that these "lacking dark matter" LSBGs could be at a closer distance than initially estimated by van Dokkum et al. (2018a, 2019a). This would not only make the stellar mass smaller (leaving room for a higher M/L fraction and therefore recovering a certain amount of dark matter, alleviating its strong deficit) but would also resolve the other anomalies that these LSBGs have related to their globular cluster luminosity function (e.g., Shen et al. 2021a), something considered a universal property of any galactic population, including LSBGs (e.g., Jordán et al. 2007; Villegas et al. 2010; Rejkuba 2012; Amorisco et al. 2018; Prole et al. 2019b). However, the distance to these galaxies is still the subject of intense debate (van Dokkum et al. 2018b; Blakeslee & Cantiello 2018; Monelli & Trujillo 2019; van Dokkum et al. 2019b; Danieli et al. 2020; Shen et al. 2021b; Zonoozi et al. 2021) and there is currently no broad consensus on these distance values, remaining

a debated range of distances between 12 and 22 Mpc approximately.

Therefore, the motivation for this work is twofold. On the one hand, we will perform a systematic detection of LSBGs with the best photometric data available in the environment of the NGC 1052 galaxy group, aiming to find new potentially interesting objects given the presence in this region of LSBGs with exotic properties. On the other hand, we will carry out an exploration of the structures that exist in this region in order to delimit the environment and study the properties of it together with the sample of LSBGs.

This article is structured as follows: in Section 2 we describe the data used, in Section 3 we present the sample and its properties. In Section 4 we carry out the analysis of the sample and in Section 5 we discuss the results. In this work we use the AB photometric system. All photometric magnitudes are extinction corrected (Schlafly & Finkbeiner 2011). We use standard cosmology with  $\Omega_m = 0.3$ ,  $\Omega_\Lambda = 0.7$  and  $H_0 = 70$  km s<sup>-1</sup> Mpc<sup>-1</sup>. The graphics of the figures are optimized for viewing in electronic version.

## 2. Data

We used photometric data from the Dark Energy Camera Legacy Survey (DECaLS; Dark Energy Survey Collaboration et al. 2016). This survey makes use of the Blanco 4m telescope, located at the Cerro Tololo Inter-American Observatory, providing wide-field multiband photometry in  $g$ ,  $r$  and  $z$  bands with a median seeing of 1.5 arcsec using the Dark Energy Camera (DECam; Honscheid & DePoy 2008). Data with this instrumentation has proven to be very efficient in searching for LSBGs (e.g., Müller et al. 2017; Tanoglidis et al. 2021; Martínez-Delgado et al. 2021a). Detailed information about DECaLS and related surveys are provided by Dey et al. (2019) and on the website<sup>1</sup>. We used publicly available data from the seventh data release (DR7).

The depth of the data in the environment of NGC 1052 is remarkable, however we found that it is not homogeneous, varying from 29.2 to 29.9 mag arcsec<sup>-2</sup> in the  $g$  band, from 28.7 to 29.1 mag arcsec<sup>-2</sup> in the  $r$  band and from 27.5 to 27.6 mag arcsec<sup>-2</sup> in the  $z$  band, all measured as  $3\sigma$  in  $10 \times 10$  arcsec boxes following the depth definition by Román et al. (2020), Appendix A. This range in depth is approximately from 0.5 to 1 mag arcsec<sup>-2</sup> deeper than the typical depth of the DECaLS data in other regions (see Martínez-Delgado et al. 2021b). It is also considerably deeper than other existing data sets in this region, for example the Sloan Digital Sky Survey (27.4 and 26.8 mag arcsec<sup>-2</sup> in the  $g$  and  $r$  bands respectively) or the Dragonfly Telephoto Array (28.9 and 28.2 mag arcsec<sup>-2</sup> in the  $g$  and  $r$  bands respectively, Abraham & van Dokkum 2014; Merritt et al. 2016) all measured as  $3\sigma$  in  $10 \times 10$  arcsec boxes. It makes the DECaLS data the most optimal for this work, approximately 1 mag deeper in  $g$  and  $r$  bands than previous works<sup>2</sup>, covering a much larger area, with better seeing and having the additional  $z$  band.

In order to explore a region wide enough to cover the environment around NGC 1052 we selected an analysis area of  $6 \times 6$  degrees, corresponding to  $2.07 \times 2.07$  Mpc at the distance of NGC 1052, which is of 20 Mpc (Tully et al. 2013). We thus explore an environment of at least 1 Mpc around NGC 1052 at its distance (the virial radius of NGC 1052 has been calculated to

<sup>1</sup> <https://www.legacysurvey.org/>

<sup>2</sup> But see very recent work by Keim et al. (2021) in the environment of NGC 1052 and Trujillo et al. (2021) in the NGC 1042 galaxy

390 kpc by Forbes et al. 2019). In coordinates this region comprises  $37.37^\circ < \text{R.A.} < 43.27^\circ$  and  $-11.26^\circ < \text{Dec.} < -5.26^\circ$ . We created these  $6 \times 6$  degree mosaics for each of the  $g$ ,  $r$  and  $z$  bands by merging individual coadd fields downloaded by querying the survey archive using a dedicated pipeline for this purpose.

### 3. The sample

#### 3.1. Detection of low surface brightness galaxies

The detection of LSBGs is usually carried out by a sequence of tasks. The first step is a broad detection of LSBGs candidates. Both the depth of the data and the efficiency of this detection in the low surface brightness regime will define the completeness of the sample, so a high efficiency in the detection of diffuse sources in this first step is a key point in the process. Given the importance of this primary detection, it is common to use specialized software or procedures (e.g., Akhlaghi & Ichikawa 2015; Prole et al. 2018; Haigh et al. 2021). After a first detection of potential objects, a characterization of their structural and morphological properties is necessary in order to accurately define the sample, typically with certain criteria in surface brightness and radius. To obtain the structural parameters of the LSBGs candidates is usual the fitting of the detected sources with a Sérsic model (Sérsic 1968). Specific procedures such as GALFIT (Peng et al. 2010) or IMFIT (Erwin 2015) are used to obtain accurate morphological and structural parameters. Per contra, the computational cost of these is very high, becoming a bottleneck in LSBGs analysis pipelines. For this reason, it is advisable to minimize the number of LSBG candidates prior to their Sérsic fitting to save computational time. However, this is not trivial since structural parameters from automated segmentation catalogues are much less accurate than Sérsic fitting modeling, making correct screening of the sample challenging. As a last step, a supervision of all objects matching the criteria of the sample is necessary in order to discard the frequent presence of false positives. These are sources that, even meeting the imposed criteria, are clearly not LSBGs. Examples of false positives are clumped sources that have been considered as a single source, faint reflections due to the optics of the instrumentation or artifacts present in the images. Depending on the data volume analyzed, the number of objects to be supervised can become very high. Due to this, it is increasingly common to use deep learning techniques to screen objects in order to eliminate these false positive detections (e.g., Tuccillo et al. 2018; Burke et al. 2019; Tanoglidis et al. 2021). However the accuracy that human visual inspection is capable of obtaining, reaching almost 100%, is not reached yet in unsupervised or automated detections. Therefore human supervision is desirable, when possible, in order to minimize the presence of false positives in the sample in reasonably limited volume data sets, as it is the case of our work.

Taking these considerations into account, we designed a pipeline for the detection of LSBGs prior to the most computationally expensive process of the Sérsic modeling. The aim of this pipeline is twofold. On the one hand, it performs a quality filtering of all sources selecting only those compatible with LSBGs, that is, extended sources with low surface brightness. On the other hand, this procedure efficiently detects objects of extreme low surface brightness. The operation of this procedure is based on the reduction of Poissonian noise by rebinning the images after masking high surface brightness objects. It allows to increase the signal to noise making diffuse sources buried in the Poissonian noise easily detectable by SExtractor (Bertin & Arnouts 1996) after a significant loss of resolution. Given the

large radius expected for the LSBGs in our sample, there is a wide margin to carry out this loss of resolution process by rebinning the pixel scale. This method of enhancing the diffuse emission by averaging small spatial scales has been used in previous works with good results (Zaritsky et al. 2019; Román et al. 2020). The operation of this pipeline is the following: We create a deep  $g + r$  image that is going to be used as a detection image. In this image we run SExtractor with a set of parameters designed for the detection of small size and high surface brightness sources and we mask all these sources in the image. Next, we rebin the masked images to  $2 \times 2$  pix, in which each pixel in the rebinned image is the average of the four original pixels, not taking into account masked values. This sequence of detecting, masking and rebinning is repeated 3 times. Starting from the original image of  $0.27''/\text{pix}$ , it produces a final  $2.16''/\text{pix}$  image in which the diffuse emission is enhanced with a significant gain of signal to noise (factor 8) with the consequent loss of resolution. We note that objects with low surface brightness do not run the risk of being masked in this process, since the detection threshold is defined well above the typical surface brightness of these objects. In Fig. 1 we show the results of this computational procedure for the different sequences or pixel scales, centred on the faintest LSBG detected in our work ( $\langle \mu_g \rangle_{\text{eff}} = 28.6 \text{ mag arcsec}^{-2}$ ).

Then, we ran SExtractor in dual mode on these enhanced images. In order to detect potential sources with a small radius, we use both  $2.16''/\text{pix}$  and  $1.08''/\text{pix}$  images for the detection. We used as detection images the  $g + r$  mosaic to measure the parameters in the  $g$  and  $r$  bands separately. At this stage, we discard the use of the much shallower  $z$  band. Among different parameters, we obtained the maximum surface brightness of the sources present in these enhanced images. These parameters, being obtained with SExtractor, do not have the precision that a Sérsic fitting provides, but given the good masking of the aforementioned process, the obtained values are robust enough to perform a source screening. We selected as LSBG candidates sources with a conservative value of  $\mu_{g,\text{max}} = 23 \text{ mag arcsec}^{-2}$  according to the value provided by SExtractor. This criterion provides a margin given that the final criterion to select the LSBGs will be a central surface brightness fainter than  $24 \text{ mag arcsec}^{-2}$  in the  $g$  band, obtained from the more accurate Sérsic fitting. The number of selected LSBG candidates matching this criterion is 335 sources. It is worth noting the great computational efficiency of this procedure, being the total computational time for this detection in the  $6 \times 6$  degrees mosaic approximately 1 hour using an AMD Ryzen 5 3600 6-core processor.

Additionally, we carried out an independent visual detection of LSBGs in the images. For that we used the great image quality in color composed images provided by the Legacy Survey browser<sup>3</sup> together with the enhanced images previously discussed. The detection was carried out by one member of the team by selecting sources with a low surface brightness but conservatively, this is selecting sources that could definitely have a higher surface brightness than the final criteria to be applied, so as not to introduce any bias that could influence detection. Since the aim of this detection is to find candidates that will finally be fitted to obtain their structural parameters with great precision, we do not make any cut in radius, that is, we exclusively select sources with diffuse brightness, again so as not to introduce any bias in this regard. The total number of sources acquired by visual inspection was 2268, leading to a total number of 2603 LSBGs candidates.

<sup>3</sup> <https://www.legacysurvey.org/viewer>



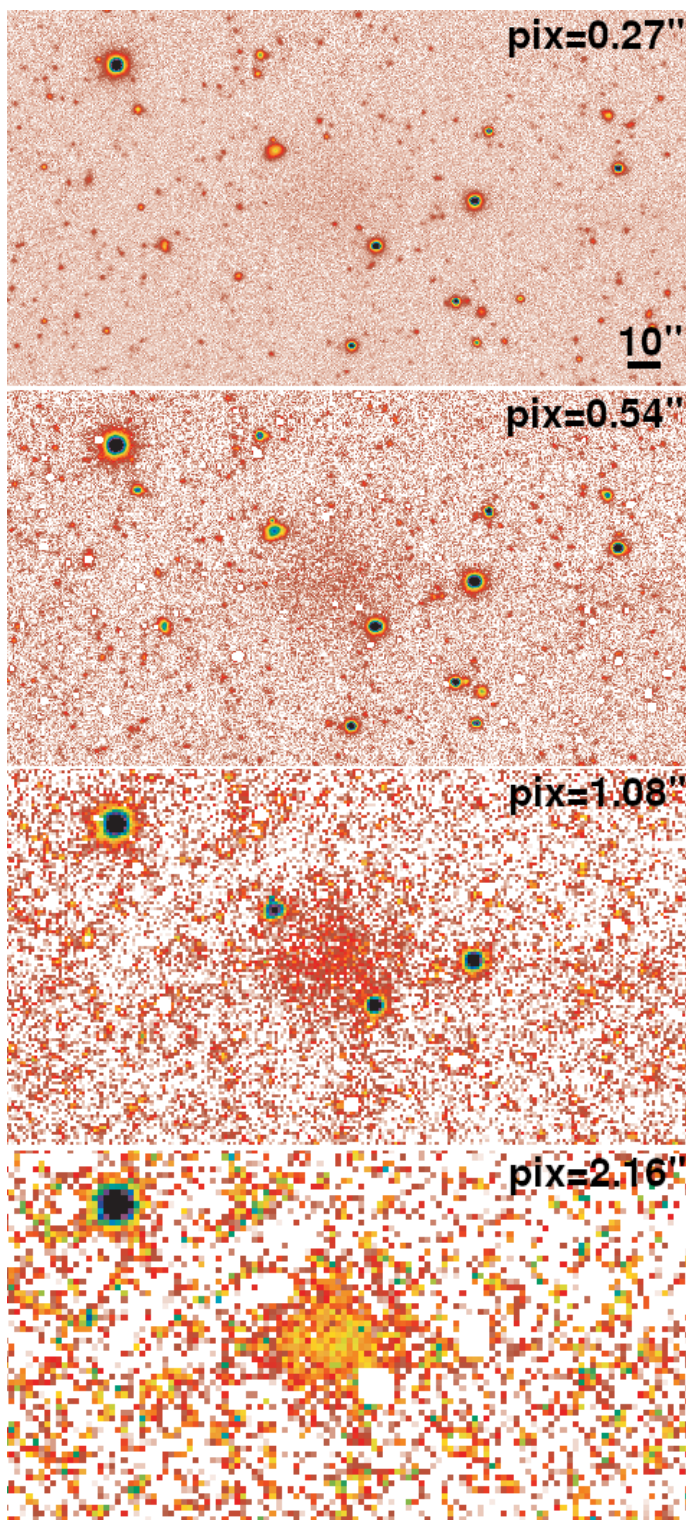


**Fig. 1.** Example of sequential masking and rebinning centred in the lowest surface brightness galaxy of the sample ( $\langle \mu_g \rangle_{eff} = 28.6 \text{ mag arcsec}^{-2}$ ). Each panel shows a stage of the rebinning process. Image detection limit is  $29.9 \text{ mag arcsec}^{-2}$  at  $3\sigma$  measured in  $10 \times 10 \text{ arcsec}$  boxes ( $g$  band).

We then obtained accurate structural and photometric parameters by fitting a Sérsic model to all the 2603 candidates. For this we use the software *IMFIT* in stamps centred on the candidate sources in which external sources have previously been masked. These stamps have the original data resolution of  $0.27''/\text{pix}$  and

the masking is performed aggressively in order to hide diffuse light from external sources. The fitting is performed in each of the available  $g$ ,  $r$  and  $z$  bands using a single Sérsic model with point spread function (PSF) deconvolution and variable sky background. The position angle and ellipticity of the target are previously calculated in the deep  $g + r$  image, and are then introduced as fixed parameters in the fitting of the individual  $g$ ,  $r$  and  $z$  bands. To obtain the PSF model we used a similar procedure to that by Román et al. (2020) and Infante-Sainz et al. (2020). It consists of making use of several unsaturated stars that after normalization and combination produce a PSF model. Since the objects to be PSF deconvolved (LSBG candidates) will be relatively small in size, we created a PSF model of  $10 \text{ arcsec}$  in radius. This is more than enough to correct for the effect of PSF on these extremely low surface brightness objects.

The selection criteria for the final sample of LSBGs is central surface brightness of  $\mu_g(0) > 24 \text{ mag arcsec}^{-2}$  and effective radius  $r_{eff} > 5 \text{ arcsec}$ , both in the deeper  $g$  band. The effective radius criterion has been chosen firstly because it is larger than that of the seeing of the observations in DECaLS ( $\approx 1.5''$ ), in addition having a balance between sources small enough to have a sample as large as possible ( $5''$  are  $\approx 500 \text{ pc}$  at the NGC 1052 distance,  $20 \text{ Mpc}$ ), but large enough to not include a significant fraction of false background projections. Applying the criteria of  $r_{eff} > 5 \text{ arcsec}$  and  $\mu_g(0) > 24 \text{ mag arcsec}^{-2}$  and after removing false detections by visual inspection (process carry out by one member of the team), we obtained a sample of 42 LSBGs. We list the final sample in Table 1. We show individual stamp images of each LSBG of the sample in Fig. 2 and we list in Table 2 their structural and photometric properties. For the designation of objects, we follow the guidelines established by the International Astronomical Union<sup>4</sup>. Since we use data for general purpose, we opted for the use of the surnames of the authors of this work (RCP), followed by the sequence number of the catalog.

Finally, a recommended procedure is to perform a completeness test, this is the fraction of statistically detected objects based on their structural parameters, typically surface brightness and radius. However in our case this is unfeasible. In the first place, because the depth of the images is variable throughout the explored area, so the detectability will vary depending on the depth of the data between different regions (and bands, given that we use for detection the  $g+r$  sum image). Additionally, the LSBG identification procedure includes a visual inspection, which is not parameterizable. For these reasons we do not provide a completeness test, however we do make a comparison with previous works.

### 3.2. Comparison with previous studies

Recent works explored the presence of LSBGs in the environment of the NGC 1052 group using deep imaging. First, Cohen et al. (2018), hereinafter Co18, explored the presence of LSBGs in a region of  $\approx 3 \times 3$  degree centred around NGC 1052 (see Section 2 for a comparative description of these data). Through a process of visual identification, Co18 reported the presence of 6 LSBGs without specific selection criteria that were later observed with the Hubble Space Telescope producing high resolution imaging. We identified in our work these 6 galaxies, see Table 1. The structural and morphological properties reported by Co18 in these 6 LSBGs are equivalent to those reported in our work. However we find an exception in the case of RCP 9 (NGC 1052-DF7): while we report an effective radius of  $12.8$

<sup>4</sup> <http://cdsweb.u-strasbg.fr/Dic/iau-spec.html>

**Table 1.** Low surface brightness galaxies with  $\mu_g(0) > 24$  mag arcsec $^{-2}$  and  $r_{eff} > 5$  arcsec detected in the large scale environment of NGC 1052. Previously identified objects are noted as identified by: <sup>a</sup> Karachentsev et al. (2000), <sup>b</sup> Paturel et al. (2003), <sup>c</sup> Whiting et al. (2007), <sup>d</sup> Cohen et al. (2018) and <sup>e</sup> Tanoglidis et al. (2021).

| ID     | RA (°)<br>(J2000) | Dec. (°)<br>(J2000) | Previous identification   |
|--------|-------------------|---------------------|---|
| RCP 1  | 37.2722           | -10.6033            | New   |
| RCP 2  | 38.2332           | -9.0575             | New   |
| RCP 3  | 38.5704           | -8.9949             | Ta21-11714 <sup>e</sup>   |
| RCP 4  | 39.0332           | -9.9845             | Ta21-11772 <sup>e</sup>   |
| RCP 5  | 39.0430           | -8.3067             | Ta21-11825 <sup>e</sup>   |
| RCP 6  | 39.2677           | -5.2661             | New   |
| RCP 7  | 39.4813           | -6.2566             | Ta21-11906 <sup>e</sup>   |
| RCP 8  | 39.5983           | -8.2217             | New   |
| RCP 9  | 39.6241           | -7.9257             | NGC 1052-DF7 <sup>d</sup>   |
| RCP 10 | 39.6952           | -6.2366             | Ta21-12088 <sup>e</sup>   |
| RCP 11 | 39.8028           | -8.1408             | NGC 1052-DF5 <sup>d</sup>   |
| RCP 12 | 39.8128           | -8.1160             | NGC 1052-DF4 <sup>d</sup>   |
| RCP 13 | 39.8270           | -7.5369             | New   |
| RCP 14 | 39.8617           | -7.3707             | New   |
| RCP 15 | 39.9104           | -7.4737             | New   |
| RCP 16 | 39.9139           | -8.2285             | Ta21-12000 <sup>e</sup>   |
| RCP 17 | 39.9696           | -8.2121             | New   |
| RCP 18 | 40.0194           | -8.4461             | NGC 1052-DF1 <sup>d</sup>   |
| RCP 19 | 40.0341           | -7.9473             | Ta21-12130 <sup>e</sup>   |
| RCP 20 | 40.0820           | -7.9847             | Ta21-12132 <sup>e</sup>   |
| RCP 21 | 40.1200           | -8.2434             | New   |
| RCP 22 | 40.1502           | -9.4977             | New   |
| RCP 23 | 40.1719           | -11.0829            | New   |
| RCP 24 | 40.1894           | -7.6470             | NGC 1052-DF8 <sup>d</sup> ; Ta21-12095 <sup>e</sup>   |
| RCP 25 | 40.2277           | -5.3300             | Ta21-12151 <sup>e</sup>   |
| RCP 26 | 40.2897           | -8.2968             | New   |
| RCP 27 | 40.3126           | -7.4934             | New   |
| RCP 28 | 40.4215           | -8.3475             | New   |
| RCP 29 | 40.4451           | -8.4028             | [KKS2000] 04 <sup>a</sup> ; LEDA 3097693 <sup>b</sup> ; NGC 1052-DF2 <sup>d</sup> ; Ta21-12200 <sup>e</sup> |
| RCP 30 | 40.4475           | -8.7854             | Ta21-12203 <sup>e</sup>   |
| RCP 31 | 40.6033           | -9.4483             | Ta21-12267 <sup>e</sup>   |
| RCP 32 | 40.6202           | -8.3768             | New   |
| RCP 33 | 40.6504           | -8.0426             | New   |
| RCP 34 | 40.6583           | -7.3381             | WHI B0240-07 <sup>c</sup>   |
| RCP 35 | 40.6963           | -7.7721             | Ta21-12129 <sup>e</sup>   |
| RCP 36 | 40.7636           | -8.0140             | New   |
| RCP 37 | 40.8702           | -7.8732             | New   |
| RCP 38 | 40.9303           | -6.9219             | Ta21-12315 <sup>e</sup>   |
| RCP 39 | 41.1604           | -7.1764             | New   |
| RCP 40 | 41.4845           | -7.6496             | New   |
| RCP 41 | 41.8189           | -8.2923             | Ta21-12521 <sup>e</sup>   |
| RCP 42 | 43.2093           | -7.8612             | Ta21-12786 <sup>e</sup>   |

arcsec, in Co18 this value is 18.9 arcsec. Regarding the properties of the 6 galaxies in common with Co18 and those unidentified, we did not find significant differences for the central surface brightness with a mean of  $\overline{\mu_g(0)} = 25.3$  mag arcsec $^{-2}$  for the galaxies in common and  $\overline{\mu_g(0)} = 25.2$  mag arcsec $^{-2}$  for those not identified by Co18. However we do find a significant difference in magnitude and effective radius, with  $\overline{g} = 18.5$  mag and  $\overline{r_{eff}} = 15.5$  arcsec for those galaxies in common with Co18 and  $\overline{g} = 19.8$  mag and  $\overline{r_{eff}} = 8.5$  arcsec for those not identified by Co18. This could be related to the higher resolution and depth of our data compared to those used by Co18. Additionally, it could be related to the Co18 identification method, not systematic with certain criteria but visually, selecting interesting targets for a high resolution follow-up by the Hubble Space Telescope.

An interesting comparison can also be made with the work by Tanoglidis et al. (2021), hereinafter Ta21, who explored the presence of LSBGs over  $\sim 5000$  deg $^2$  from the first three years of imaging data from the Dark Energy Survey (DES), including the region of the NGC 1052 environment that we explore in our work. The criteria to define a LSBG according to Ta21 are  $r_{eff} > 2.5$  arcsec and  $\langle \mu_g \rangle_{eff} > 24.2$  mag arcsec $^{-2}$ , therefore less restrictive in terms of effective radius than our LSBG criteria. We found that 17 of the 42 galaxies identified in our work appear in the Ta21 catalogue, see Table 1. The structural and photometric properties reported by Ta21 on these 17 galaxies in common are similar to what we report here. However we found a small difference for the central surface brightness, in which the values in our work are on average 0.15 mag

**Table 2.** Structural and photometric parameters of the sample

| ID     | $r_{eff}$<br>[arcsec] | $\mu_g(0)$<br>[mag arcsec <sup>-2</sup> ] | $<\mu_g>_{eff}$<br>[mag arcsec <sup>-2</sup> ] | $n$       | b/a       | $g$<br>[mag] | $g-r$<br>[mag] | $g-z$<br>[mag] |
|--------|-----------------------|---|--|-----------|-----------|--------------|----------------|----------------|
| RCP 1  | 6.0±2.1               | 25.9±0.2                                  | 27.0±0.5                                       | 0.95±0.55 | 0.71±0.07 | 21.17±0.11   | 0.63±0.20      | 1.06±0.26      |
| RCP 2  | 5.4±0.9               | 26.5±0.3                                  | 27.0±0.5                                       | 0.51±0.33 | 0.82±0.13 | 21.33±0.11   | 0.57±0.22      | 0.37±0.38      |
| RCP 3  | 8.3±0.5               | 25.0±0.1                                  | 25.8±0.3                                       | 0.69±0.09 | 0.81±0.02 | 19.17±0.02   | 0.58±0.03      | 0.80±0.05      |
| RCP 4  | 6.0±0.4               | 24.2±0.1                                  | 25.7±0.4                                       | 0.90±0.16 | 0.45±0.02 | 19.82±0.03   | 0.72±0.05      | 0.97±0.08      |
| RCP 5  | 5.2±0.3               | 24.5±0.1                                  | 25.3±0.4                                       | 0.66±0.11 | 0.71±0.03 | 19.75±0.02   | 0.31±0.04      | 0.42±0.07      |
| RCP 6  | 9.2±4.5               | 26.3±0.2                                  | 27.2±0.4                                       | 0.78±0.48 | 0.86±0.09 | 20.35±0.14   | -              | -              |
| RCP 7  | 10.8 ±0.3             | 24.1±0.1                                  | 25.2±0.2                                       | 0.90±0.06 | 0.75±0.01 | 18.02±0.01   | 0.51±0.02      | 0.64±0.03      |
| RCP 8  | 5.6 ±2.4              | 26.2±0.2                                  | 27.5±0.5                                       | 1.05±0.50 | 0.61±0.11 | 21.80±0.10   | 0.39±0.22      | 1.07±0.39      |
| RCP 9  | 12.8 ±1.5             | 25.9±0.2                                  | 27.3±0.2                                       | 0.71±0.18 | 0.51±0.03 | 19.73±0.04   | 0.45±0.08      | 0.81±0.15      |
| RCP 10 | 8.1 ±1.1              | 24.5±0.1                                  | 25.8±0.3                                       | 1.14±0.21 | 0.81±0.03 | 19.24±0.03   | 0.68±0.05      | -              |
| RCP 11 | 10.0 ±0.8             | 25.9±0.2                                  | 26.5±0.3                                       | 0.55±0.12 | 0.84±0.04 | 19.51±0.05   | 0.64±0.18      | 0.95±0.15      |
| RCP 12 | 16.8 ±0.4             | 24.3±0.1                                  | 25.2±0.1                                       | 0.80±0.04 | 0.86±0.01 | 17.07±0.01   | 0.63±0.01      | 1.06±0.02      |
| RCP 13 | 11.0 ±0.7             | 25.4±0.1                                  | 26.2±0.2                                       | 0.75±0.12 | 0.85±0.03 | 19.02±0.02   | 0.49±0.04      | 0.78±0.06      |
| RCP 14 | 12.3 ±4.1             | 26.9±0.4                                  | 27.8±0.3                                       | 0.61±0.35 | 0.68±0.07 | 20.36±0.17   | -              | -              |
| RCP 15 | 8.1 ±0.8              | 25.6±0.1                                  | 26.8±0.3                                       | 0.63±0.18 | 0.50±0.03 | 20.29±0.04   | 0.56±0.08      | 0.50±0.18      |
| RCP 16 | 6.1 ±0.7              | 24.3±0.1                                  | 25.6±0.4                                       | 0.82±0.19 | 0.56±0.02 | 19.63±0.02   | 0.55±0.05      | 0.77±0.06      |
| RCP 17 | 6.4 ±4.0              | 26.6±0.3                                  | 27.9±0.5                                       | 1.14±0.50 | 0.53±0.17 | 21.52±0.16   | 0.84±0.54      | 1.01±0.45      |
| RCP 18 | 24.7 ±6.2             | 26.3±0.2                                  | 27.9±0.7                                       | 1.10±0.35 | 0.72±0.05 | 18.90±0.65   | -              | -              |
| RCP 19 | 8.6 ±0.5              | 24.6±0.1                                  | 25.7±0.3                                       | 0.88±0.11 | 0.75±0.02 | 18.99±0.02   | 0.49±0.03      | 0.81±0.05      |
| RCP 20 | 6.8 ±0.2              | 24.1±0.1                                  | 25.0±0.3                                       | 0.77±0.07 | 0.77±0.02 | 18.84±0.01   | 0.55±0.02      | 0.86±0.04      |
| RCP 21 | 8.9 ±1.9              | 26.0±0.2                                  | 26.9±0.4                                       | 0.74±0.26 | 0.79±0.17 | 20.17±0.07   | 0.55±0.16      | -              |
| RCP 22 | 5.2 ±1.0              | 25.5±0.1                                  | 26.6±0.4                                       | 0.59±0.35 | 0.52±0.06 | 21.01±0.05   | 0.80±0.12      | 1.29±0.15      |
| RCP 23 | 9.9 ±1.2              | 25.5±0.1                                  | 26.6±0.3                                       | 0.86±0.20 | 0.76±0.03 | 19.59±0.05   | 0.66±0.08      | 0.95±0.12      |
| RCP 24 | 7.1 ±0.3              | 25.0±0.1                                  | 25.6±0.3                                       | 0.58±0.08 | 0.80±0.03 | 19.37±0.02   | 0.35±0.04      | 0.35±0.09      |
| RCP 25 | 6.4 ±0.8              | 24.8±0.1                                  | 25.7±0.4                                       | 0.87±0.22 | 0.85±0.04 | 19.69±0.04   | 0.64±0.06      | 0.96±0.09      |
| RCP 26 | 9.1 ±0.6              | 24.7±0.1                                  | 25.9±0.3                                       | 0.77±0.13 | 0.63±0.02 | 19.08±0.02   | -              | -              |
| RCP 27 | 6.8 ±0.6              | 25.5±0.1                                  | 26.5±0.4                                       | 0.69±0.19 | 0.66±0.05 | 20.35±0.07   | 0.57±0.11      | 0.94±0.40      |
| RCP 28 | 7.1 ±1.7              | 26.1±0.2                                  | 27.0±0.5                                       | 0.78±0.37 | 0.74±0.08 | 20.79±0.17   | 1.05±0.37      | -              |
| RCP 29 | 21.3 ±0.3             | 24.7±0.1                                  | 25.3±0.1                                       | 0.58±0.02 | 0.89±0.01 | 16.62±0.01   | 0.60±0.01      | 0.94±0.01      |
| RCP 30 | 7.6 ±0.3              | 24.4±0.1                                  | 25.3±0.3                                       | 0.71±0.07 | 0.72±0.02 | 18.94±0.02   | 0.63±0.03      | 0.86±0.05      |
| RCP 31 | 6.5 ±0.5              | 24.7±0.1                                  | 25.9±0.4                                       | 0.74±0.14 | 0.54±0.02 | 19.84±0.03   | 0.56±0.06      | 0.95±0.08      |
| RCP 32 | 23.0 ±7.5             | 27.8±0.7                                  | 28.6±0.5                                       | 0.50±0.36 | 0.70±0.07 | 19.75±0.41   | -              | -              |
| RCP 33 | 9.9 ±0.5              | 25.3±0.1                                  | 26.0±0.3                                       | 0.77±0.10 | 0.88±0.03 | 19.06±0.03   | 0.46±0.08      | 0.69±0.18      |
| RCP 34 | 17.8 ±0.1             | 24.1±0.1                                  | 24.7±0.1                                       | 0.46±0.01 | 0.82±0.01 | 16.41±0.01   | 0.35±0.01      | 0.46±0.01      |
| RCP 35 | 8.6 ±0.3              | 24.3±0.1                                  | 25.5±0.3                                       | 0.82±0.08 | 0.61±0.01 | 18.85±0.01   | 0.50±0.03      | 0.80±0.04      |
| RCP 36 | 6.7 ±0.6              | 25.5±0.1                                  | 26.5±0.3                                       | 0.45±0.15 | 0.49±0.03 | 20.39±0.02   | 0.41±0.06      | 0.62±0.11      |
| RCP 37 | 7.0 ±0.8              | 25.9±0.2                                  | 27.0±0.3                                       | 0.60±0.23 | 0.57±0.05 | 20.75±0.03   | 0.72±0.07      | 1.22±0.12      |
| RCP 38 | 8.4 ±0.6              | 25.5±0.1                                  | 26.2±0.3                                       | 0.61±0.12 | 0.82±0.03 | 19.57±0.03   | 0.58±0.05      | 1.16±0.08      |
| RCP 39 | 11.2 ±0.3             | 24.1±0.1                                  | 25.6±0.2                                       | 0.79±0.05 | 0.45±0.01 | 18.37±0.01   | 0.42±0.03      | 0.61±0.04      |
| RCP 40 | 6.4 ±0.3              | 24.1±0.1                                  | 25.2±0.3                                       | 0.82±0.10 | 0.70±0.03 | 19.16±0.01   | 0.42±0.02      | 0.65±0.04      |
| RCP 41 | 5.5 ±0.3              | 24.5±0.1                                  | 25.5±0.4                                       | 0.75±0.12 | 0.72±0.03 | 19.76±0.02   | 0.46±0.03      | 0.76±0.06      |
| RCP 42 | 5.9 ±1.1              | 25.3±0.1                                  | 26.6±0.4                                       | 0.91±0.36 | 0.49±0.05 | 20.80±0.05   | 0.54±0.12      | 0.97±0.16      |

arcsec<sup>-2</sup> brighter than those found by Ta21. Given that magnitude, effective radius and Sérsic index are similar between both catalogs, we attribute this difference to the PSF deconvolution process that we do in the Sérsic model fit, not carried out by Ta21. We find significant differences in average parameters between galaxies in common and those not detected by Ta21 in our sample. The LSBGs in our catalogue not detected by Ta21 are on average fainter ( $\bar{g} = 19.8$  vs. 19.2 mag), larger ( $\bar{r}_{eff} = 10.4$  vs. 8.1 arcsec) and with a significantly lower surface brightness ( $\bar{\mu}_g(0) = 25.7$  vs. 24.6 mag arcsec<sup>-2</sup>) than those LSBGs in our catalog in common with Ta21. In turn, there are 10 galaxies with the criteria of  $r_{eff} > 5$  arcsec and  $\mu_g(0) > 24.0$  mag arcsec<sup>-2</sup> that are found in the Ta21 catalogue but not in ours. We found that 8 of these 10 galaxies were preliminary identified in the identification process with parameters very close to the selection criteria but not fulfilling it:

4 were discarded for having  $r_{eff} < 5$  arcsec and 4 for having  $\mu_g(0) > 24.0$  mag arcsec<sup>-2</sup>. Of the 2 remaining objects, we considered one of them to have multiple components, so it would have been discarded in the visual inspection criteria (object\_id = 11784 in Ta21; R.A. = 38.6509, Dec. = -10.9843) and another object that was undetected by our procedure (object\_id = 2752 in Ta21; R.A. = 37.2745, Dec. = -10.6457).

### 3.3. Properties of the low surface brightness galaxies

In Fig. 3 we plot the distributions of the most relevant structural and photometric properties of the LSBG sample. The Sérsic indexes show a clear distribution centered on  $n = 0.77$  with a standard deviation of  $\sigma = 0.22$ , with only 4 objects exceeding  $n = 1$ . This distribution in Sérsic index is compatible with a sample whose criterion is the central surface brightness (Koda et al.



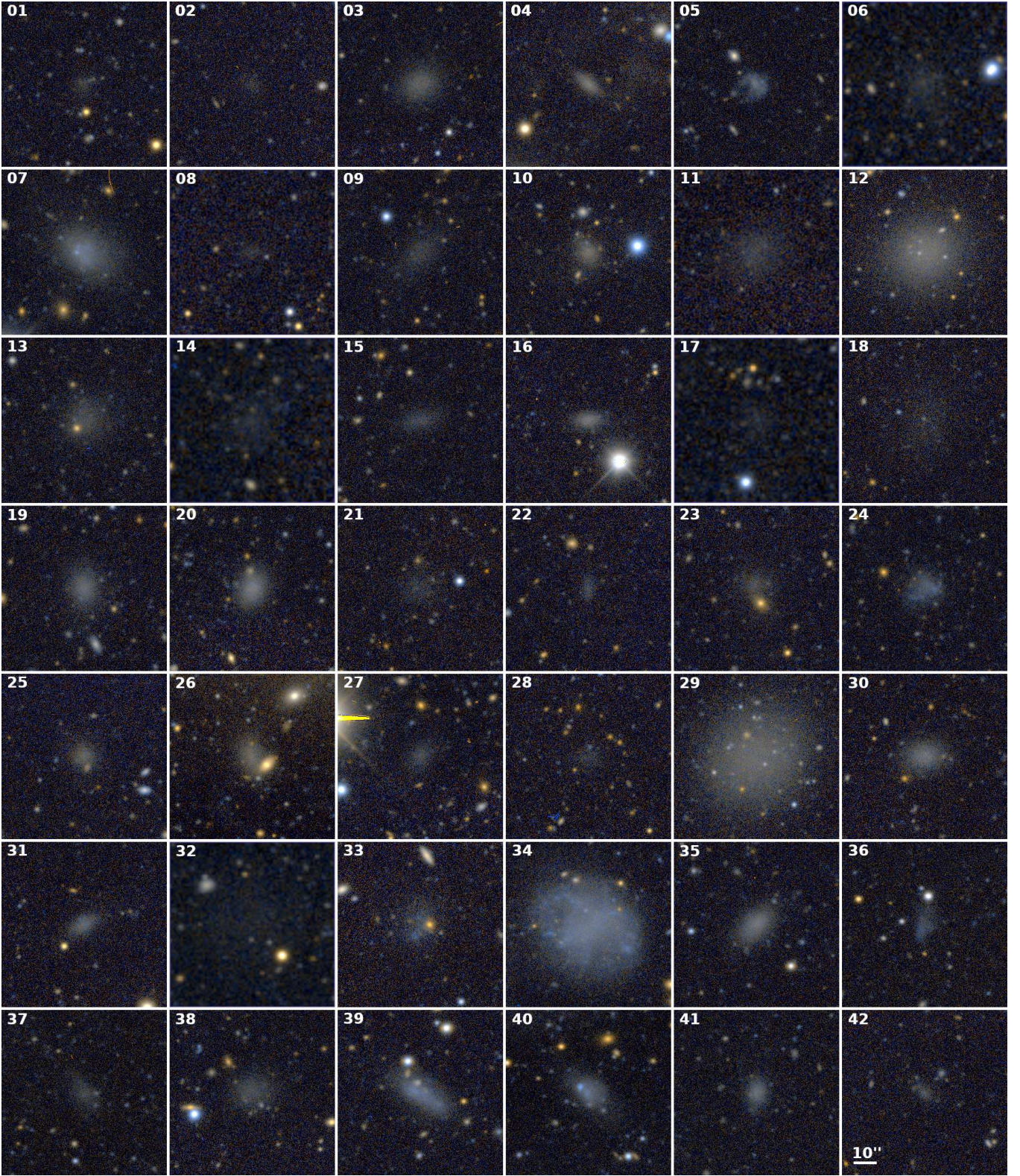


**Fig. 2.** Color-composed images with  $g$  and  $r$  bands of all LSBGs in the sample. The size of the stamps is 81 arcseconds, north up and east left. The images of the fainter galaxies have been smoothed with a Gaussian kernel to enhance contrast. The ID catalogue number (see Table 1) is placed in the upper left corner of each LSBG.

2015; Román & Trujillo 2017a). In turn, the surface brightness distributions show behaviors consistent with the selection criteria. The central surface brightness shows an approximately constant distribution up to approximately  $\mu_g(0) > 26.5$  mag arcsec<sup>-2</sup>. Two objects have extremely low surface brightness (RCP 14

and RCP 32). The distribution is more homogeneous in the case of the average surface brightness within the effective radius, as expected, with galaxies ranging between  $\langle\mu_g\rangle_{eff} = 25$ -28 mag arcsec<sup>-2</sup> with the two previously mentioned objects having  $\langle\mu_g\rangle_{eff} > 28$  mag arcsec<sup>-2</sup>. Regarding effective radii, we



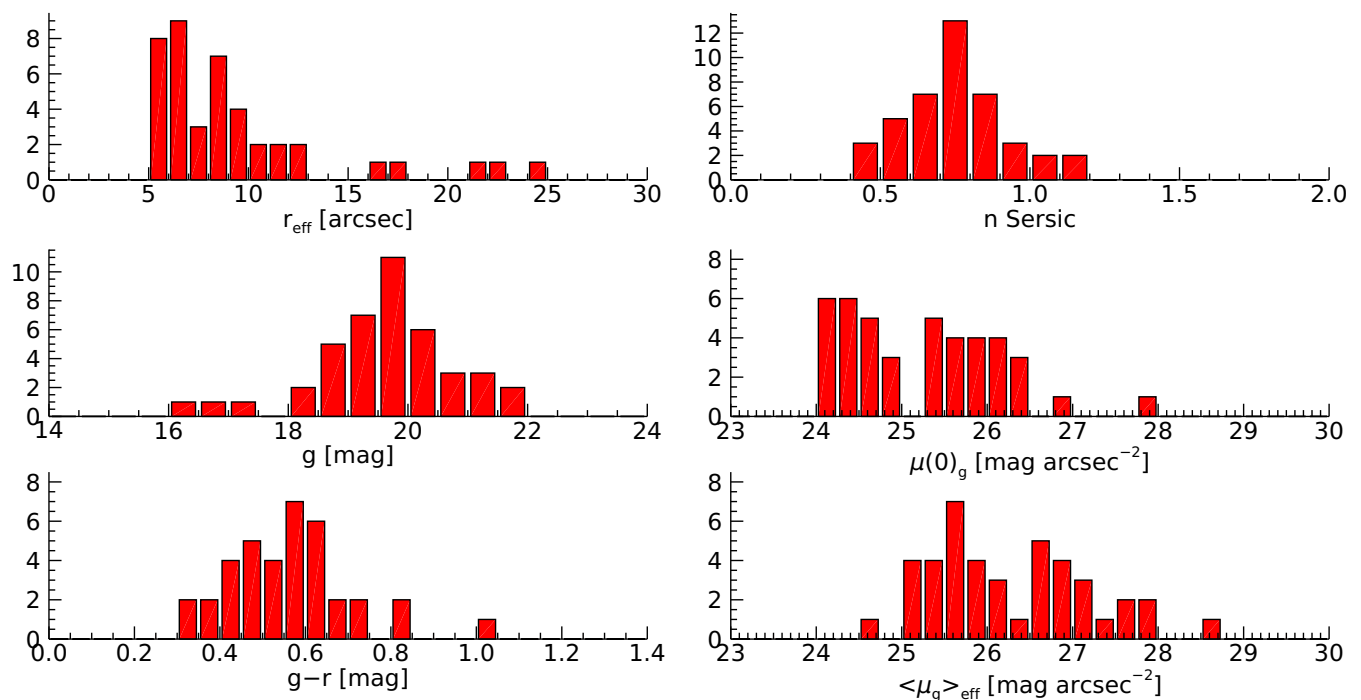


**Fig. 3.** Histograms of structural and photometric properties of the sample.

find a compact distribution up to 15 arcsec. Above this value we find a number of galaxies that have an effective radius larger than the continuity of the distribution. The apparent magnitude distribution in the  $g$  band is well centred at a value of  $g = 19.6$  mag, with a standard deviation of  $\sigma = 1.2$  mag. Finally, the analysis of the  $g-r$  color (we ruled out the use of the  $z$  band due to its shallow depth) has the potential of showing the presence of sources projected in the background, reddened, that are not physically associated with the structure of interest in the analysis, in our case the environment of the group of galaxies of NGC 1052. While the histogram of the  $g-r$  color shows objects that have a value higher than  $g-r = 0.7$ , taking into account the photometric errors, listed in Table 2, all LSBGs in the sample have a  $g-r$  compatible with  $g-r < 0.7$  mag within photometric errors. Therefore no object can be considered a projection in the background based on the photometric colors (we note, however, that not all objects have a  $g-r$  color value because of lower signal-to-noise in the  $r$  band compared to the  $g$  band, see Table 2). This is expected since the criterion of  $r_{\text{eff}} < 5$  arcsec is effective in selecting very close objects, and therefore not reddened. Due to the large photometric uncertainties in these extremely low surface brightness objects, we ruled out the use of photo- $z$  in the analysis.

## 4. Analysis

### 4.1. Potential globular clusters in the LSBGs

The analysis of globular clusters (GCs) is of great interest in the study of LSBGs. These have the potential to provide relatively accurate distance estimations (e.g., Rejkuba 2012) and are tracers of the dynamical mass of the host galaxy once their radial velocities have been calculated (e.g., Beasley et al. 2016). We have carried out a statistical analysis for the presence of GC systems around the detected LSBGs. The main difficulty in detecting GCs is the high confusion that exists between them and point sources both in background and foreground. The use of high-resolution, multi-band photometric data is helpful in reduc-

ing the interloper fraction. In our case, the ground based resolution with an average seeing of approximately 1 arcsec and the availability of the  $g$ ,  $r$  and  $z$  allows a significant reduction in the fraction of false detections, although not total. Therefore, in the absence of spectroscopic measurements only a statistical analysis is feasible with the available data. In this situation, an overdensity of sources compatible with GCs over the area where the LSBG is located would indicate the presence of a GC system, but no individual sources can be confidently claimed to be GCs.

In order to constrain the properties of potential GCs in the LSBGs of our sample, we used the spectroscopically confirmed GCs of RCP 12 (NGC1052-DF4) and RCP 29 ([KKS2000] 04, NGC1052-DF2) provided by (van Dokkum et al. 2018c; Em-sellem et al. 2019; van Dokkum et al. 2019a; Shen et al. 2021a), with a total of 24 GCs. The photometric and structural parameters of these confirmed GCs in our data will provide a template for selecting GC candidates in other galaxies.

The characterization of the GCs was carried out by performing aperture photometry using SExtractor in dual mode, with the  $g+r$  sum image for detection and the individual  $g$ ,  $r$  and  $z$  bands for photometry. This is done on individual stamps of 4 arcmin centred on the LSBGs in the catalog. For the photometry of point sources, we selected an aperture of 12 pixels or 3.24 arcsec (approximately  $3 \times \text{FWHM}$  or seeing of the data) and a detection threshold of  $5\sigma$  with the aim of selecting high signal to noise sources. The resulting parameters for the confirmed GCs of RCP 12 and RCP 29 are shown in Fig. 4. Of the 24 spectroscopically confirmed GCs in the sample, we detected 21 in our data. As can be seen, the GCs have typical colors well constrained in the  $g-r$  vs  $r-z$  map with an average color of  $g-r = 0.6$  mag and  $r-z = 0.3$  mag. However the fainter ones appear with larger photometric errors, and in some cases, outside this main region in the  $g-r$  vs  $r-z$  map. The structural properties also appear well limited. The FWHM of the GCs are equivalent to the seeing of the data, around 1.2 arcsec in the  $g$  band and 1.1 arcsec in the  $r$  band, and they therefore appear as point-like or unresolved sources in our ground-based data. The ellipticity of the



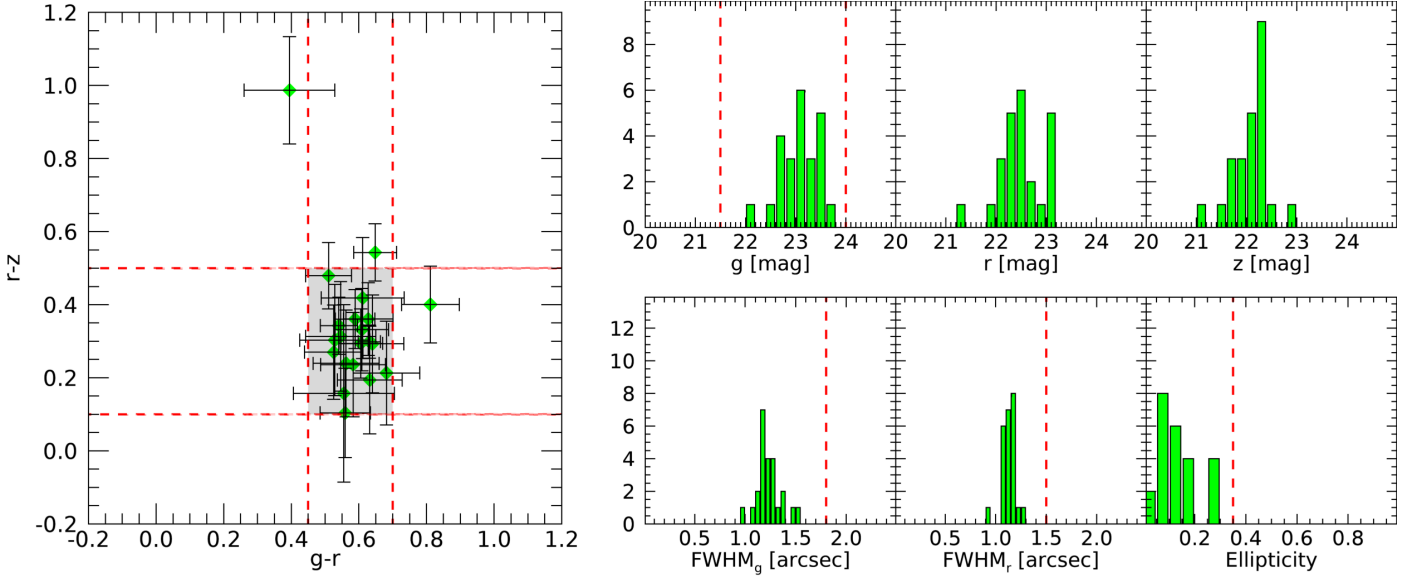


**Fig. 4.** Properties of spectroscopically confirmed globular clusters by previous works in the galaxies RCP 12 (NGC 1052-DF4) and RCP 29 (NGC 1052-DF2) in our data. The left panel shows the colors of the GCs in the  $g-r$  vs  $r-z$  map. The right panels show histograms with their photometric and structural properties. The dashed red lines show the criteria for the detection of new GC candidates for the galaxies in our sample.

GCs remains below 0.35. All of these properties are compatible with those found in previous works using high-resolution space data from the Hubble Space Telescope.

We used the photometric and structural ranges in which the spectroscopically confirmed GCs are located to delimit the parameters of potential GCs in the LSBGs of our catalog. In particular, we selected a color range of  $0.45 < g-r < 0.7$ ,  $0.1 < r-z < 0.5$ , indicated in Fig. 4 (left panel) by the red dashed lines and the shaded area. We limited the FWHM in the  $g$  band to 1.8 arcsec and in  $r$  band to 1.5 arcsec to select point-like sources while taking into account possible seeing variations throughout the large area explored. It is expected that different regions were observed at different epochs, and therefore with different seeing. Finally, we limited the ellipticity of the sources to 0.35. We performed aperture photometry in the stamps where the Sérsic model of the LSBGs has been subtracted, aiming to obtain the cleanest possible point source photometry.

As discussed above, a GCs system would appear as an overdensity of GC candidates on the LSBGs with respect to a statistical background of interlopers. This is analyzed in two complementary ways. First, we plot in Fig. 5 the number of GC candidates per unit area in bins of annular apertures centred on each of the LSBGs of our sample. This is done using 0.45 arcmin step annular apertures in the same way for all LSBGs. Additionally, given that there are significant differences for the sizes of the LSBGs, we created a parameter, which we call  $\beta$ , that takes into account the effective radii of the LSBGs to calculate a possible overdensity located within the value of 3 times the effective radius for each galaxy, which we define as:

$$\beta = \frac{GC_{cand}[R < 3 \times r_{eff}]}{GC_{cand}[R > 3 \times r_{eff}]}. \quad (1)$$

This is the fraction of GC candidates per unit area within the  $3 \times r_{eff}$  region divided by the number of candidates per unit area outside of this region. We used  $3 \times r_{eff}$  as a value in which most of the GCs are expected to be located, if they exist, motivated by the work by Forbes (2017); Saifollahi et al. (2021). With this  $\beta$  parameter we take into account the size of each LSBG to obtain

a possible overdensity of GC candidates on it. It is worth noting that according to this criterion, to claim a detection ( $\beta > 1$ ) at least 1 GC candidate must be found within  $3 \times r_{eff}$ , and additionally, the number of GC candidates per unit area must be higher within  $3 \times r_{eff}$ . In the case that no GC candidate is detected within  $3 \times r_{eff}$ ,  $\beta = 0$  will be obtained, and we will conclude the absence of a GC system. In the case of obtaining a  $\beta$  value close to 1, this would just be compatible with a background of false detections.

The results of this analysis are the clear detection of a high density of GC candidates in the galaxies RCP 12 and RCP 29, with  $\beta$  values well above the unity, something of course expected. We also detected an overdensity of GC candidates in RCP 32, with  $\beta = 1.7$ . These three LSBGs are the only ones in which a non-zero  $\beta$  value is obtained. The  $\beta$  value in RCP 32 is significantly lower than in RCP 12 and RCP 29, indicating fewer potential GCs. The profile of GC candidates per unit area in RCP 32 is similar to that of RCP 12 and RCP 29, with a decreasing number as the radius grows, from the central region to approximately a distance of 5 effective radii. This confirms that the overdensity of GC candidates over RCP 32 behaves reliably.

In this analysis we can also find LSBGs with  $\beta = 0$  but with a considerable number of GC candidates at larger distances. After analyzing in detail the particular cases we found that some are pure statistical fluctuations, however we also found that for some LSBGs, which are very close to other massive galaxies, the GC candidates belong to the adjacent massive galaxy. Clear examples of this situation are RCP 26, located very close to NGC 1052, and RCP 40, located on the periphery of NGC 1084. Undoubtedly, the GCs belonging to these massive galaxies are clearly detectable with our criteria, having been studied in previous works as in the case of NGC 1052 (Pierce et al. 2005).

According to our analysis, the only GCs systems detected in our sample are the already known ones in RCP 12 and RCP 29, and the marginal detection of a GCs system in RCP 32. In Fig. 6 we show color stamps of these galaxies along with the spectroscopically confirmed GCs by previous works that are detected in our data (in red). Additionally, we show the GC candidates that appear after applying the photometric criteria discussed above (in green). As can be seen in RCP 12 and RCP 29, despite only

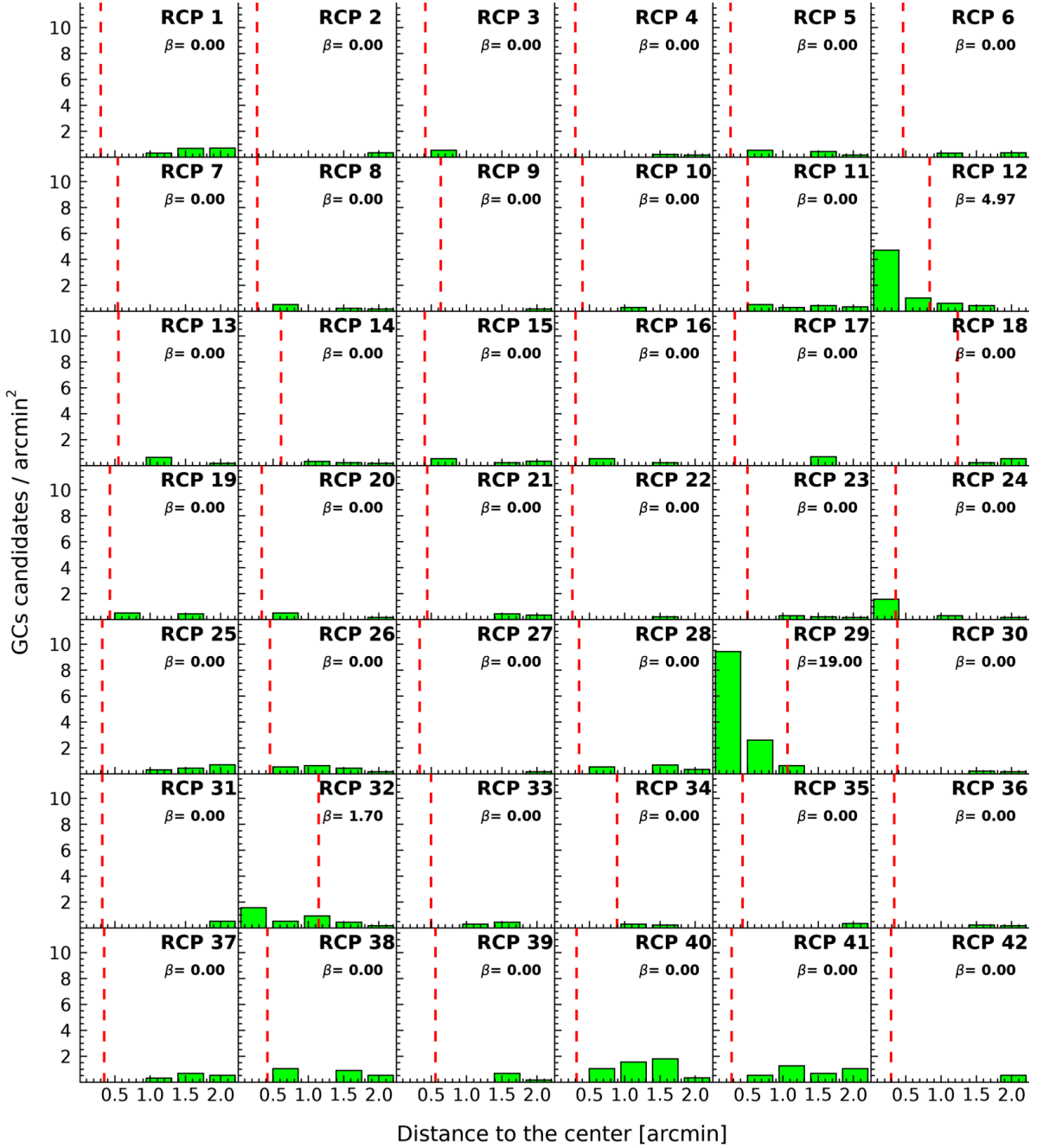


**Fig. 5.** Number of GC candidates per unit area in circular profiles centered on the LSBGs of our sample. Histograms show the values for each bin in radius of the profile. The dashed red line shows the  $3 \times r_{\text{eff}}$  value for each galaxy. The  $\beta$  value is shown for each galaxy (see main text).

having ground-based observations in  $g$ ,  $r$  and  $z$  bands, the GC candidates trace the distribution of spectroscopically confirmed GCs remarkably well, with a low fraction of false detections. This efficient filtering of GCs against false detections strongly favor considering the GCs system detected in RCP 32 as real.

We note that the photometric criteria used for the detection of GC candidates are those corresponding to the specific GC population of RCP 12 and RCP 29 galaxies, and similar between both. Therefore, it is possible that the stellar populations in the case of RCP 32, or another LSBG in the sample, were significantly different. Hence the criteria based on the already detected populations of GCs in RCP 12 and RCP 29 may not be as effective in other galaxies in the sample. Better resolution data and

with the inclusion of the important  $u$  band could be more decisive in the search for GCs in the LSBGs.

One of the striking properties of RCP 12 and RCP 29 galaxies, and a source of controversy, is that if they were located at the distance of NGC 1052, 20 Mpc, the GCs would be more luminous (e.g., van Dokkum et al. 2018a; Shen et al. 2021a) than the expected given the universality of the globular cluster luminosity function (GCLF) in galaxies (Rejkuba 2012). It is therefore worth exploring whether this also occurs in RCP 32. First, we measured the peak of the luminosity function of the spectroscopically confirmed GCs in our data. These values calculated as the average value of the detected GCs are:  $\mu_g = 23.16$  mag,  $\mu_r = 22.52$  mag and  $\mu_z = 22.05$  mag for RCP 12 and  $\mu_g = 23.01$  mag,  $\mu_r = 22.48$  mag and  $\mu_z = 22.21$  mag for

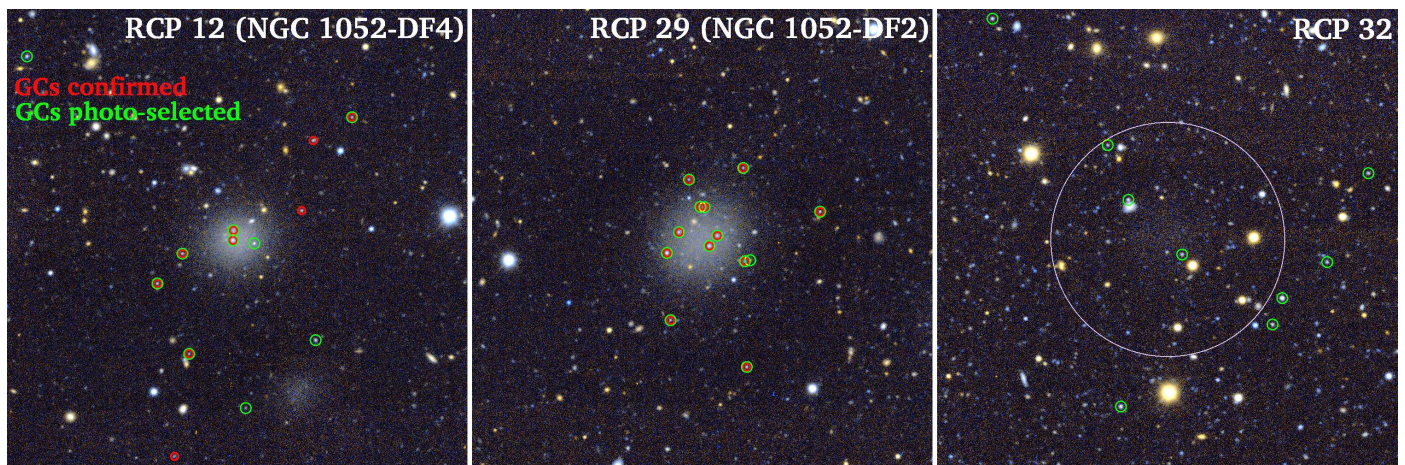


**Fig. 6.** Color-composed stamps using the  $g$  and  $r$  bands centered on the 3 low surface brightness galaxies in which we detect a globular clusters system. Stamps are 4 arcmin on a side. The spectroscopically confirmed globular clusters in RCP 12 (NGC 1052-DF4) and RCP 29 (NGC 1052-DF2) galaxies that are detectable in our data are marked with red circles. The globular clusters that appear after applying our photometric criteria are marked by green circles. We place a purple circle marking  $3 \times r_{\text{eff}}$  on RCP 32 easing the visualization due to appearing barely visible in this color stamp.

RCP 29. We note here that the peak calculated in our data is slightly lower than the equivalent of previous works since we are missing a few GCs that are not detected because of the point source detection limit of our data, lower than that of the Hubble Space Telescope used in previous works. However it is useful for direct comparison in RCP 32:  $\mu_g = 23.15$  mag,  $\mu_r = 22.52$  mag and  $\mu_z = 22.35$  mag. We can verify that the GC candidates of RCP 32 have a peak in their luminosity function equivalent to those of RCP 12 and RCP 29, suggesting that it would be at a similar distance, around 13 Mpc, if the GCLF peak method applies in these galaxies (see Trujillo et al. 2019). We warn here, since the GCs of RCP 32 are not spectroscopically confirmed, so a certain presence of false GCs is expected. It could have a significant impact given the low number of GC candidates for the calculation of the peak of the GCLF in RCP 32.

#### 4.2. Spatial correlation with spectroscopic line-of-sight structures

An intrinsic problem with very low surface brightness sources is the systematic absence of spectroscopic measurements with which to obtain their distances. Due to this, it is necessary to include in any environmental analysis the possibility of false projections in the LSBG sample, and therefore the need to study spatial structures at different distances in the projected line of sight. To characterize the structures present in the analyzed field, we used the NASA/IPAC Extragalactic Database (NED) to obtain spectroscopic measurements available in the region. We carried out a search in a  $8 \times 8$  deg region, 1 deg wider in each side than the LSBGs detection mosaic in order to trace possible structures that are adjacent to the LSBGs, but outside the boundaries where detection of LSBGs was carried out. This region is therefore  $36.37^\circ < \text{R.A.} < 44.27^\circ$ ,  $-12.26^\circ < \text{Dec.} < -4.26^\circ$ . We used for this task the search by parameters in NED, unselecting spectroscopy of HII regions or different components of galaxies.

In Fig. 7 we show the histogram of galactic redshifts that we obtained from the NED database in the previously discussed selected area. There is a peak with a considerable number of galaxies (35 objects, including RCP 29 or NGC 1052-DF2, see Table 1) with a similar radial velocity to that of NGC 1052 ( $z = 0.005$ ). We mark in the histogram a gray region which can

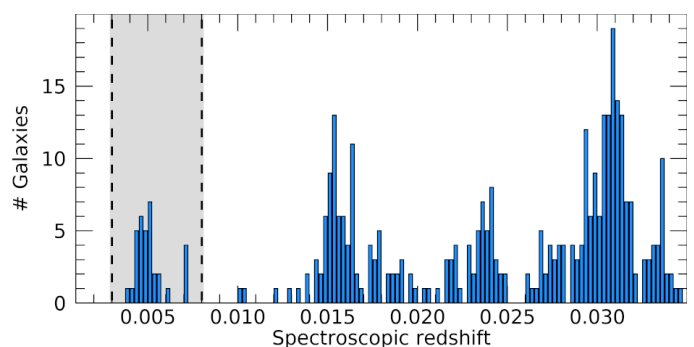


**Fig. 7.** Histogram of galaxies with spectroscopic redshift in the analyzed region. The gray shaded stripe marks the structure of interest associated with the NGC 1052 group of galaxies at  $0.003 < z < 0.008$ , corresponding to  $\approx 900 < V_{\text{rad}} < 2400$  km s $^{-1}$ .

be considered the redshift interval associated with the environment of NGC 1052 ( $0.003 < z < 0.008$ ), and therefore the region of interest in this work. We note the existence of a virialized-looking structure of 31 galaxies in the interval  $0.004 < z < 0.006$  with calculated velocity dispersion of  $\sigma = 135$  km s $^{-1}$  whose mean radial velocity is 1453 km s $^{-1}$ , very similar to the radial velocity of NGC 1052 of 1510 km s $^{-1}$ . We find also a sub-group at approximately  $z = 0.007$  with a velocity dispersion of  $\sigma = 12$  km s $^{-1}$  centered at a radial velocity of 2114 km s $^{-1}$ . We put in Table A.1 the name, coordinates and radial velocities of all the galaxies with spectroscopy in this region. The NGC 1052 environment is considerably isolated in redshift space. We found a void region at  $0.007 < z < 0.013$ , finding the first clearly virialized background structure at  $z = 0.015$ , and a more massive structure at  $z = 0.031$ . This isolation in redshift space, along with being the first structure in the foreground, ensures a low fraction of interlopers or false background projections for the LSBGs in the NGC 1052 environment. Nevertheless, it is interesting to explore the spatial correlation of the detected LSBGs with the spectroscopic galaxies in different redshift slices in order to draw their spatial correlation.

In Fig. 8 we plot the spatial distribution of the detected LSBGs with the galaxies with spectroscopy located in the inter-



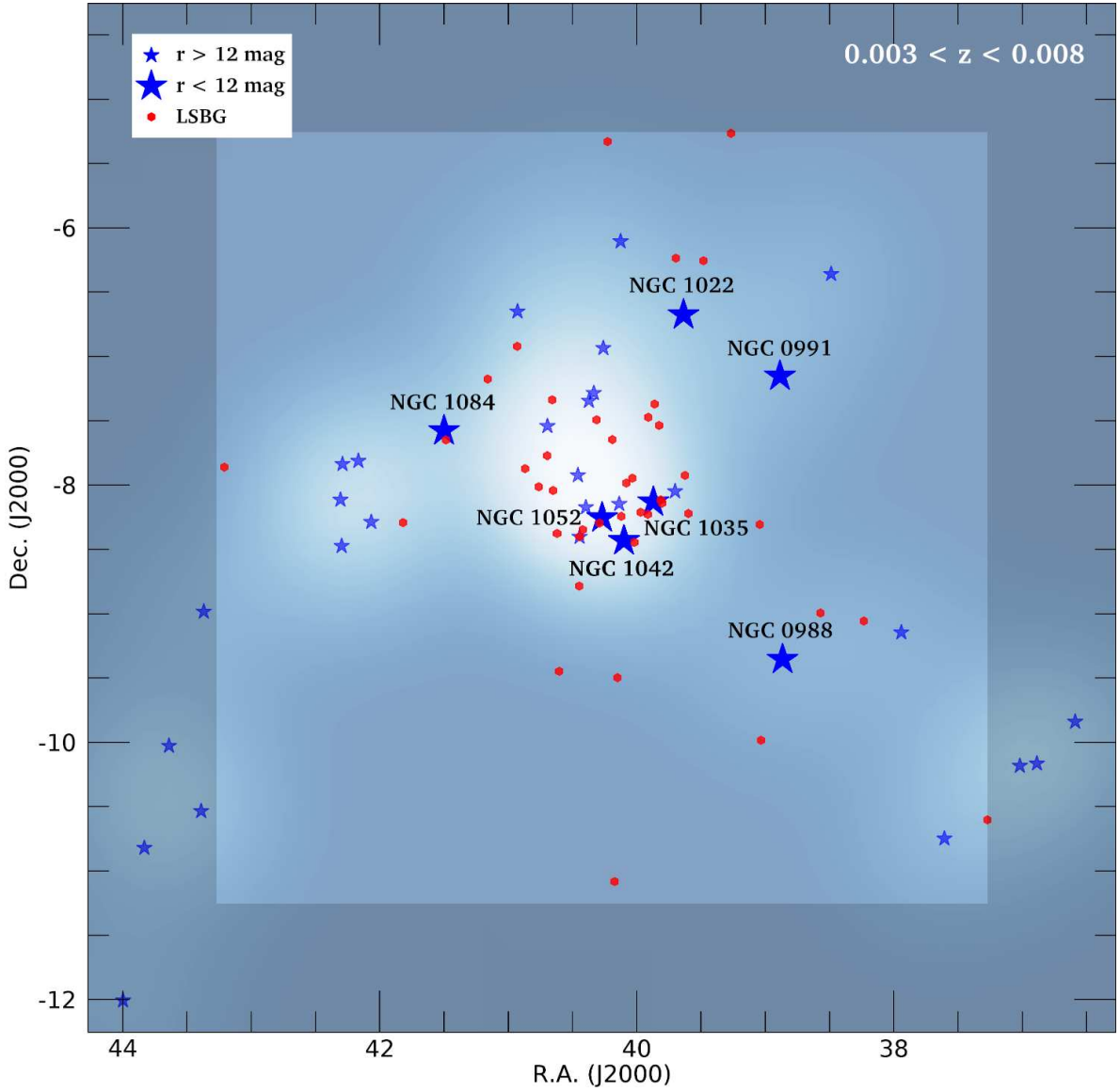


**Fig. 8.** Spatial correlation of the LSBGs (red dots) together with galaxies with spectroscopic measurements (blue stars) in the interval  $0.003 < z < 0.008$  to which the NGC 1052 environment belongs. Galaxies with spectroscopy are differentiated between having a magnitude greater or less than  $r = 12$  mag. The shaded region marks the limit where an identification of LSBGs has not been carried out but galaxies with spectroscopy are included, for a better characterization of the large-scale structure. A white background traces the density of galaxies with spectroscopy for ease of visualization.

val  $0.003 < z < 0.008$ . We differentiate between galaxies with a magnitude higher or lower than  $r = 12$  mag, which is useful to identify the most massive or dominant galaxies in the region. There is a well-defined large-scale structure centred in the analyzed area. We place the names of these dominant galaxies in Fig. 8. In the center of this structure are 3 galaxies with  $r < 12$  mag: NGC 1052, NGC 1042 and NGC 1035. Around these 3 dominant galaxies there is the highest concentration of LSBGs. Surrounding this denser central region are a number of spectroscopic galaxies, including some massive galaxies with  $r < 12$  mag. However, the densities of both spectroscopically confirmed galaxies and LSBGs are low in these outer regions. We can also find regions with a total absence of galaxies. In general, we can affirm that the spatial correlation of the LSBGs with the galaxies located in the redshift interval associated with the NGC 1052 environment is good.

For comparison, we have carried out the same analysis, this time with galaxies in the background of the environment of NGC 1052 ( $0.008 < z < 0.035$ ), which can be visualized in the Fig. 9. We have included 3 maps similar to that of Fig. 8 corresponding to the overdensities observed at  $0.008 < z < 0.020$ ,  $0.020 < z < 0.025$  and  $0.025 < z < 0.035$  separately, and a fourth panel which corresponds to the cumulative of the three ( $0.008 < z < 0.035$ ). Visual inspection of these maps allows us to verify that the spatial correlation between LSBGs and galaxies in the redshift range in which NGC 1052 is found is higher than the spatial correlation with background structures. It is interesting to note that the probability that a LSBG belongs to a structure in the background decreases with its distance, because the number density of LSBGs with a given radius decreases with radius (Koda et al. 2015; Román & Trujillo 2017a). For this reason, a cut like the criterion of  $r_{eff} > 5$  arcsec that we use in our work tends to select the more nearby objects.

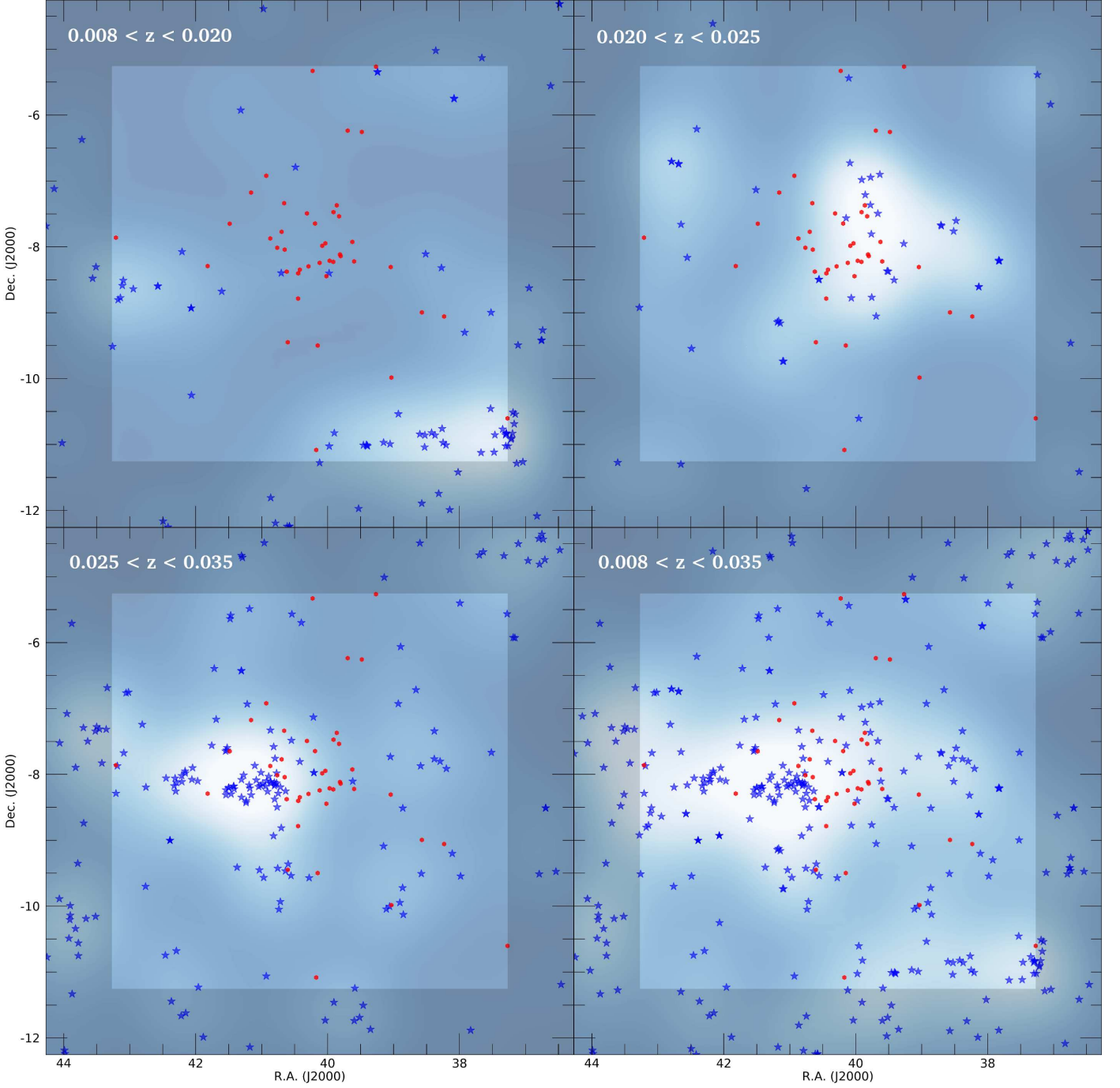


**Fig. 9.** Similar plot to that of Fig. 8 but in different redshift intervals corresponding to overdensities in the background of the NGC 1052 environment, for each panel. We note that the bottom right panel ( $0.008 < z < 0.035$ ) is the cumulative of the other three panels.

In order to confirm our results quantitatively we provide here a characterization of the spatial correlation of the structure through statistical parameters. We measure the spatial distribution of galaxies in two-dimensions as projected on to the plane of the sky. This can be studied through the two dimensional projected angular correlation function  $\omega(\theta)$ , which is defined through the expression

$$dP = N^2 [1 + \omega(\theta)] d\Omega_1 d\Omega_2 \quad (2)$$

where  $N$  represents the surface density per squared radian and  $d\Omega_1$ ,  $d\Omega_2$  are infinitesimal solid angles separated by an angle  $\theta$ . This equation represents the probability with respect to a

Poissonian distribution of finding two galaxies with an angular separation  $\theta$ . The usual estimation for  $\omega(\theta)$  is given by the ratio of the number of pair of galaxies counted in the sample to that expected from a random distribution with the same mean density and sampling geometry.

The statistical characterization of the spatial correlation calculated here comprised two steps. First the two-point angular correlation function was studied to compare cluster properties and identify the group whose statistical parameters are most compatible with those from LSBGs. In the second step the two-point angular cross-correlation function (CCF) was calculated. Due to the low number density, the first step gave inconclusive

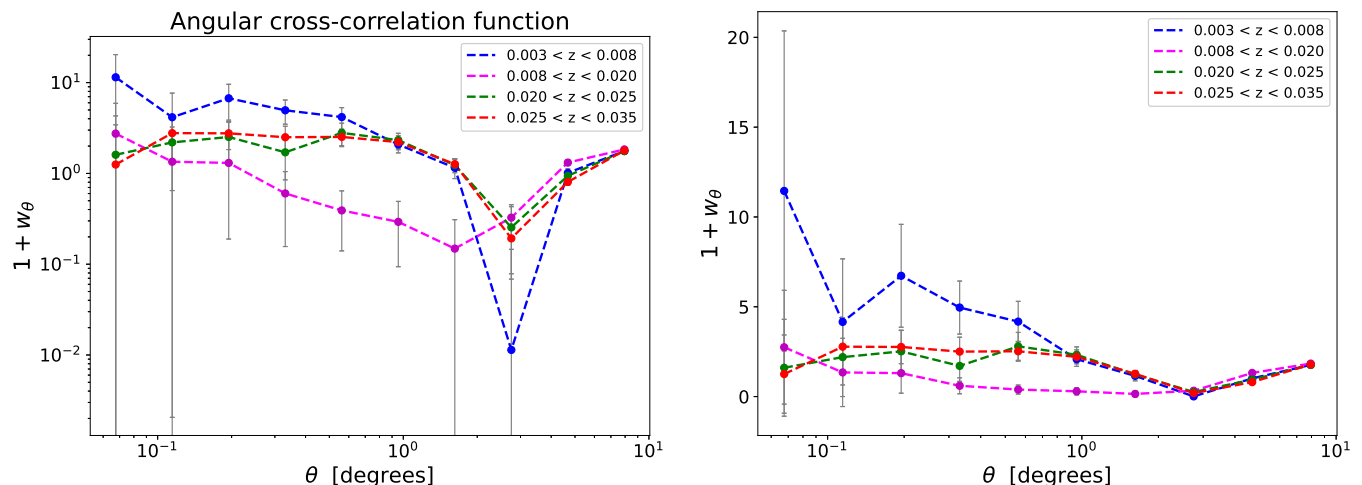


**Fig. 10.** Two-point angular cross-correlation function for LSBGs and galaxies with different redshift intervals. Left panel is in log-log scale. Right panel shows the two-point angular CCF in semilog scale for visualization purposes.

results so we limited the study to the two-point angular CCF between LSBGs and each of the groups of galaxies.

Using the samples of LSBGs and galaxies with estimated redshift described previously, we create 10.000 random samples (no noticeable difference was found when using 100,000) and we calculate the LSBGs-group two-point angular CCF following (Croft et al. 1999). We used the correlation function implemented in `mock_observables` sub-package from `Halotools` v0.7 (Hearin et al. 2017) as described as:

$$1 + w(\theta) \equiv DD(\theta)/RR(\theta), \quad (3)$$

where  $DD(\theta)$  and  $RR(\theta)$  are the number of sample pairs and of random pairs with separations equal to  $\theta$  respectively.

In Eq. 3 we used the Landy-Szalay correction (Landy & Szalay 1993) to the pair counts which is more unbiased than the natural method and produce a nearly poissonian variance. Errors are estimated through a self-made<sup>5</sup> algorithm performing bootstrap re-sampling of the two-point angular CCF. A collection of 50 randomized catalogs populating the same sky coverage as the data are generated by bootstrap. The error is, then, estimated through the standard deviation for the statistic of the resulting set.

The two-point angular CCF thus obtained is calculated for a number of bins corresponding to angular distances in degrees. The size of the bin will be determined in general by the sample size. In our case we calculated the two-point angular CCF with several spatial bins spaced logarithmically from 0.05 to 10 deg. For hierarchical structures a decreasing trend of  $1 + \omega(\theta)$  with radius (i.e.  $\theta$ ) is expected.

Fig. 10 shows the two-point angular CCF for LSBGs and galaxies corresponding to each of the redshift peaks identified. Note that for  $0.05 < \theta < 1.0$  the angular cross-correlation is higher for the first peak than for the rest. This is the interval where the highest density of galaxies is found so it is the most relevant range to calculate the statistics. For smaller angular distances the density is too small (zero counts in some cases), for larger angular distances the two-point angular CCF converges.

<sup>5</sup> see [github.com/javier-iaa/LSBGs\\_1052\\_paper/Two\\_Point\\_Angular\\_Cross-Correlation\\_Function.ipynb](https://github.com/javier-iaa/LSBGs_1052_paper/Two_Point_Angular_Cross-Correlation_Function.ipynb) for details on the calculation

These results indicate a higher spatial correlation between LSBGs and galaxies with spectroscopic measurements located in the  $0.003 < z < 0.008$  interval. Taking into account this correlation and that the number of LSBGs is expected to decrease strongly with distance when applying a selection cut in  $r_{eff} > 5$  arcsec, it suggests that the majority of LSBGs detected are associated with the structure located at the redshift interval  $0.003 < z < 0.008$  to which NGC 1052 belongs. We note, however, the infeasibility of distance estimates in individual galaxies, and only a statistical study of the complete sample of LSBGs is possible through this analysis.

#### 4.3. Spatial distribution of outlier LSBGs in effective radius

In Section 3.3 we analyzed the properties of the LSBG sample. We identified an anomalous effective radius distribution in which we find a number of LSBGs with high outlier values in relation to the main declining distribution. In this section we explore this issue.

In Fig. 11 we plot the LSBGs with an effective radius smaller (left panel) and larger (right panel) than  $r_{eff} = 15$  arcsec, together with the distribution of galaxies with spectroscopy located at the  $0.003 < z < 0.008$  interval, in the same way as performed in Fig. 8. As can be seen, the LSBGs with an effective radius larger than 15 arcsec are located compactly in the central region where the galaxy NGC 1052 is located. On the contrary, when plotting LSBGs with an effective radius less than 15 arcsec, the LSBGs are homogeneously distributed over the entire region. We plot in Fig. 12 the correlation between the effective radius of the LSBGs against their distance in angular projection from NGC 1052 ( $D_{NGC1052}$ ). We find that LSBGs located nearby in projection from NGC 1052 have, on average, higher effective radius:  $\langle r_{eff} \rangle = 12.2 \pm 1.9$  arcsec for  $D_{NGC1052} = [0, 0.5]$  deg and  $\langle r_{eff} \rangle = 9.3 \pm 1.0$  arcsec for  $D_{NGC1052} = [0.5, 1.0]$  deg, while we find  $\langle r_{eff} \rangle = 7.3 \pm 0.5$  arcsec for  $D_{NGC1052} > 1$  deg. Another way of looking at this is by exploring the values of  $D_{NGC1052}$  that LSBGs with higher effective radius have versus those with lower effective radius. We find that for LSBGs with  $r_{eff} > 15$  arcsec we obtain  $\langle D_{NGC1052} \rangle = 0.48 \pm 0.14$  deg against  $\langle D_{NGC1052} \rangle = 1.25 \pm 0.15$  deg for LSBGs with  $r_{eff} < 15$  arcsec.

These results show a statistically significant anomaly in which the LSBGs that have outlier values in the distribution of



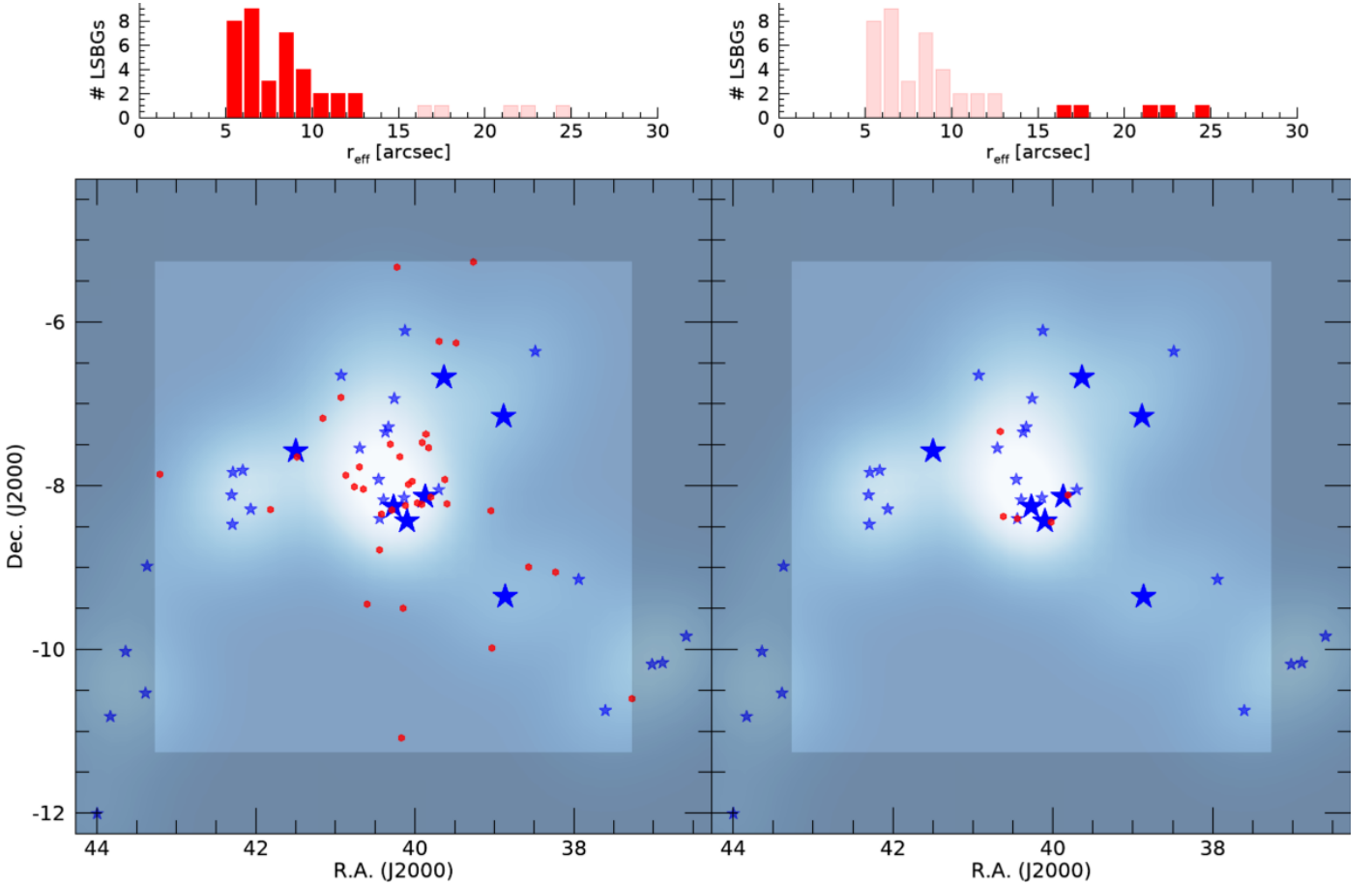


**Fig. 11.** Spatial distribution of LSBGs and galaxies with spectroscopic measurements at  $0.003 < z < 0.008$  similar to that of Fig. 8. Here, LSBGs are plotted separately with  $r_{\text{eff}} < 15$  arcsec (left panel) and  $r_{\text{eff}} > 15$  arcsec (right panel). In the upper part of both panels, the distribution of effective radii of the LSBGs is presented with dark red for the galaxies plotted in their lower panel and light red for the hidden ones.

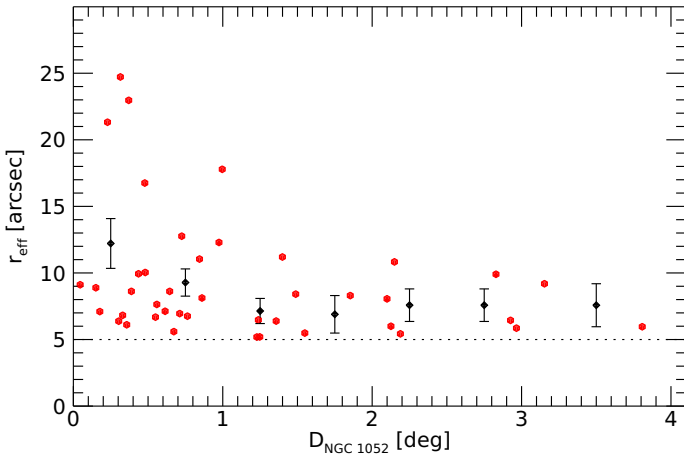


**Fig. 12.** Correlation between the effective radius of the LSBGs and their projected distance to the NGC 1052 galaxy in red points. The black points with bars show the mean and the error in the mean in each bin of distance. The dotted line marks the detection limit of LSBGs of  $r_{\text{eff}} = 5$  arcsec.

effective radii with  $r_{\text{eff}} > 15$  arcsec are clustered in the most central area explored, where NGC 1052 and the highest concentration of galaxies are located. This difference in effective radii is significant, almost doubling the mean value in  $D_{\text{NGC}1052}$

$< 0.5$  deg for the LSBGs than that found in peripheral regions of  $D_{\text{NGC}1052} > 1$  deg.

## 5. Discussion

In this work we have carried out an exhaustive and systematic detection of low surface brightness galaxies in the environment of the galaxy NGC 1052. Photometric data from the Dark Energy Camera Legacy Survey and a dedicated pipeline for the detection of extremely faint objects have allowed us to expand the catalog of LSBGs in this region with 20 new objects of 42 of our catalogue. Among all the new objects, RCP 32 stands out with extreme properties:  $r_{\text{eff}} = 23.0$  arcsec and  $\langle \mu_g \rangle_{\text{eff}} = 28.6$  mag arcsec $^{-2}$ . This extremely low surface brightness makes RCP 32 one of the lowest surface brightness galaxies ever detected by integrated photometry, maybe only surpassed by the object BST1047+1156 located in the Leo I group (Mihos et al. 2018). The clear presence of RCP 32 in the processed images by our pipeline with relatively high signal to noise (see Fig. 1), the presence in both  $g$  and  $r$  bands (the  $z$  band is not deep enough), the marginal presence in other data sets<sup>6</sup> and its overdensity of GC candidates, all confirm that RCP 32 is a real object and not an artifact or reflection from nearby stars in the images. The fact that RCP 32 has remained undetected so far is remarkable given that NGC 1052-DF2, located at just 10 arcmin in projection (see

<sup>6</sup> RCP 32 appears marginally detected in the deep images by Müller et al. (2019) and Keim et al. (2021).

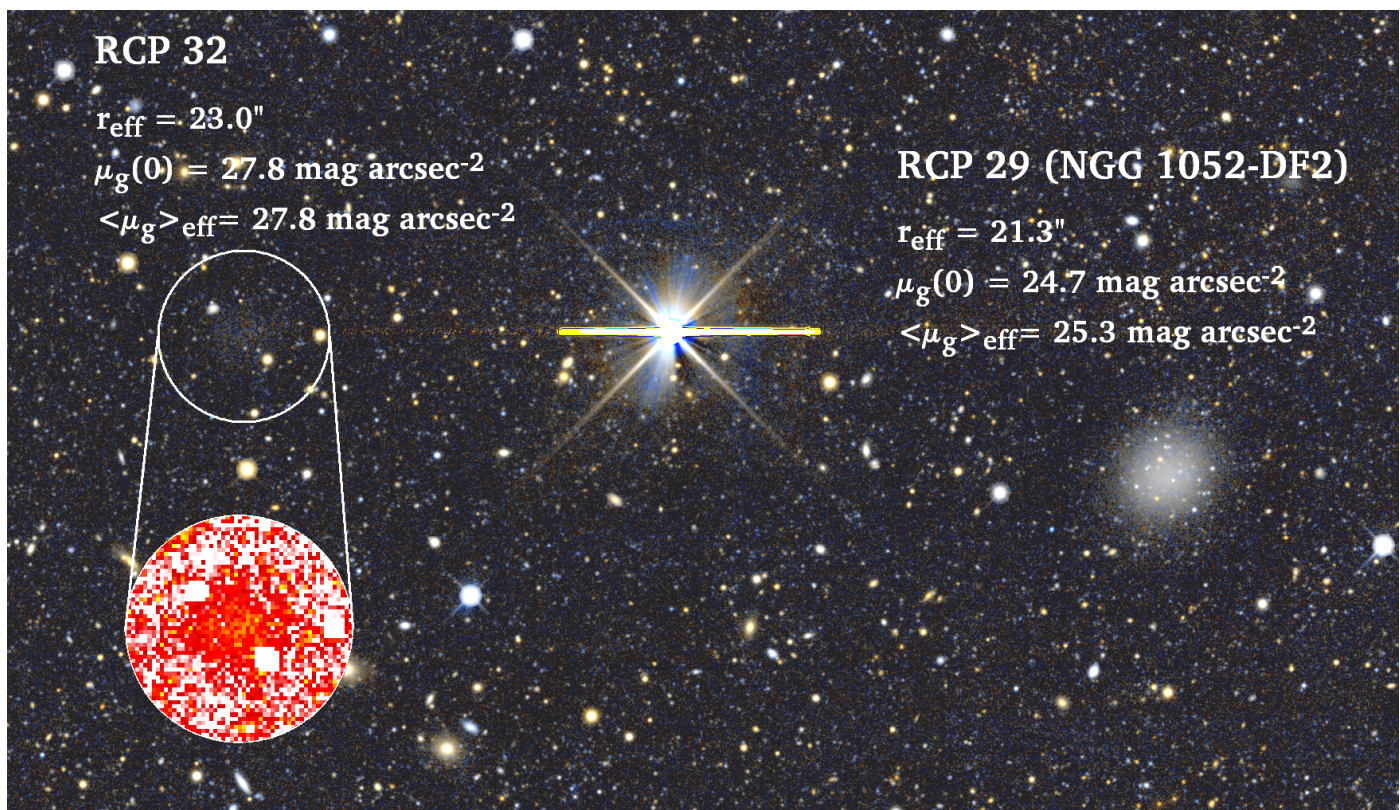


**Fig. 13.** Color-composed image using the  $g$  and  $r$  bands of a field showing the proximity between RCP 32 and RCP 29 (NGC 1052-DF2). Given the low surface brightness of RCP 32, we placed a zoom-in circle showing the processed image in which LSBGs were detected to improve the visualization of the galaxy (see Section 3.1).

Fig. 13), is a galaxy extensively observed and analyzed in recent years. It highlights the importance of deep data and an adequate photometric processing to bring out the structures with the lowest surface brightness.

Our analysis of the available spectroscopy in this region has identified a structure at a redshift range of  $0.003 < z < 0.008$  with a size of approximately 1 Mpc in diameter assuming the distance of 20 Mpc at which NGC 1052 is located (Tully et al. 2013). The spatial distribution of the detected LSBGs correlates strongly with this structure, having a lower spatial correlation with the structures identified in the background of the redshift space. LSBGs are usually low-mass galaxies, so they tend to be satellites of more massive galaxies, therefore, a spatial correlation can be expected. However, isolated or field LSBGs are also often found (e.g., Prole et al. 2021). The expected correlation between density and morphology of low-mass galaxies in group environments (e.g., Weinmann et al. 2006; Kazantzidis et al. 2011) might improve our study performed in Sect. 4.2 through bayesian analysis by including the morphology factor in the prior distribution.

However, before conducting a more sophisticated study on the spatial correlation, certain unknowns related with the redshift-independent distances in this region must be clarified. In particular, there is a debate about the distances at which the galaxies RCP 12 (NGC 1052-DF4) and RCP 29 (NGC 1052-DF2) are located, which is crucial in determining the amount of dark matter on these. If located at a distance of 20 Mpc, similar to that of NGC 1052, the stellar mass of these would be comparable to the dynamical mass (van Dokkum et al. 2018a, 2019a). However, Trujillo et al. (2019); Monelli & Trujillo (2019); Zonoozi et al. (2021) claim a significantly closer distance, which would al-

leviate the anomalies of these galaxies related to their dark matter content, and also their overluminous population of GCs (van Dokkum et al. 2018c; Shen et al. 2021a).

Certainly, our work provides observational clues that are interesting in this discussion. The analysis carried out in section 4.3 shows that the effective radii of the LSBGs in our sample have a clear dependence on the environment, in which LSBGs located close to NGC 1052 tend to be much larger. Previous works analyzing the correlation between the effective radii and the environment for LSBGs or dwarf galaxies show inconsistent results with each other (Janz et al. 2016; Román & Trujillo 2017a; Venhola et al. 2019; Mancera Piña et al. 2019; Choque-Challapa et al. 2021; Kadowaki et al. 2021). Even focusing on only those studies that find such a correlation, this correlation is very weak, with variations of the average values of the effective radius across different environmental densities of only a small fraction. In the case of our work, this increase is very strong, almost doubling the mean values of effective radii in regions close to NGC 1052. Therefore, the strong variations of the effective radii for LSBGs in the NGC 1052 environment can be considered an anomaly.

The existence of a significant number of LSBGs with larger apparent sizes in a region of the space is a clear indication of a bimodality in the distances for the detected LSBGs. In fact, given that the galaxy NGC 1042 is located at a distance of around  $\approx 13$  Mpc (Theureau et al. 2007; Monelli & Trujillo 2019), closer than the larger structure associated with NGC 1052 at 20 Mpc, this is somehow expected. An important point here is that among the LSBGs that form this anomaly, RCP 12 (NGC 1052-DF4) and RCP 29 (NGC 1052-DF2) are included, which would imply that



they are likely components of this closer structure in the line of sight.

Recent works by Montes et al. (2020) and Keim et al. (2021) have shown evidence of tidal interactions in RCP 12 (NGC 1052-DF4) and RCP 29 (NGC 1052-DF2). It is interesting to explore whether this anomaly in the sizes of the LSBGs could be related to the tidal distortions caused by the central galaxy NGC 1052. Under this hypothesis, one can ask what makes the environment of NGC 1052 special for creating such expansion of the sizes of the LSBGs by tidal interactions but not in any other similar group of galaxies. One explanation could be the one addressed by Keim et al. (2021) in which the absence or deficit of dark matter in RCP 12 (NGC 1052-DF4) and RCP 29 (NGC 1052-DF2) makes them more susceptible to being tidally disturbed. However, this would lead to other problems. The first one is that not only RCP 12 (NGC 1052-DF4) and RCP 29 (NGC 1052-DF2) do appear with larger sizes in the vicinity of NGC 1052, but there are 5 LSBGs with an outlier effective radius in this region. This would cause the need to find a common characteristic to all of them that will explain their susceptibility to being tidally disturbed, and therefore appearing with larger sizes. Additionally, the tidal interactions observed in RCP 12 (NGC 1052-DF4) and RCP 29 (NGC 1052-DF2)<sup>7</sup> appear as small deformations on the outskirts of these galaxies, something that in any case would not explain such a dramatic increase in the effective radius. Also, this hypothesis would not produce an immediate explanation for the overluminosity of the GCs observed in RCP 12 (NGC 1052-DF4) and RCP 29 (NGC 1052-DF2), which is another anomaly to take into account in the discussion. Further studies or models regarding effects from tidal interactions, assuming a deficiency in dark matter for the LSBGs, would be interesting, maybe explaining all these circumstances in a common scenario.

Indeed, GCs are of crucial importance in this discussion, and the potential GC system detected in RCP 32 could be of high interest. It seems to have a peak of its GCLF similar in luminosity to those of RCP 12 (NGC 1052-DF4) and RCP 29 (NGC 1052-DF2), and therefore overluminous if located at 20 Mpc. We note that RCP 32 is also one of the LSBGs in our sample with  $r_{eff} > 15$  arcsec. Assuming stellar properties for RCP 32 similar to those of RCP 29 (NGC 1052-DF2) with age = 8.9 Gyr and  $[M/H] = -1.1$  (Fensch et al. 2019; Ruiz-Lara et al. 2019) the stellar mass for RCP 32 would be  $M_{\star} = 1.5 \times 10^7 M_{\odot}$  at 20 Mpc or  $M_{\star} = 6.1 \times 10^6 M_{\odot}$  at 13 Mpc. This is of the order of one tenth of the stellar mass of RCP 12 (NGC 1052-DF4) or RCP 29 (NGC 1052-DF2). Given its low baryon content and its diffuse morphology, it is difficult to understand that RCP 32 could exist without the presence of a significant amount of dark matter. The mass threshold for survival of dark matter-poor dwarf galaxies is estimated to be around  $10^8 M_{\odot}$  (Bournaud & Duc 2006). Since no HI is detected in RCP 32, only the presence of dark matter would allow self-gravitation and long-term survival, so the presence of dark matter seems necessary. This scenario is, of course, speculative, but if the overluminosity of their GCs and the presence of dark matter are confirmed, being located at 20 Mpc this would be a counterexample to affirm that in the cases of RCP 12 (NGC 1052-DF4) and RCP 29 (NGC 1052-DF2) the overluminosity of their GCs is related to their absence of dark matter (e.g., Trujillo-Gomez et al. 2021a,b; Lee et al. 2021).

Finally, direct distance measurements for RCP 12 (NGC 1052-DF4) and RCP 29 (NGC 1052-DF2) using the tip of the red giant branch method have also been debated,

reaching different results even through the use of identical data (see Cohen et al. 2018; van Dokkum et al. 2018b) vs. (Trujillo et al. 2019; Monelli & Trujillo 2019). It is worth noting here the latest results using data of exceptional depth from the Hubble Space Telescope by Danieli et al. (2020) in NGC 1052-DF4 and Shen et al. (2021b) in NGC 1052-DF2. These works find a distance of approximately 20 Mpc, and therefore suggesting that these galaxies would have indeed a strong deficit of dark matter and a overluminous population of GCs. One of the points made by these works is that the blending of sources by crowding could have a significant impact for the calculation of the tip. It is interesting to note that in the case of RCP 32, given its extremely low surface brightness, the crowding effect would be very low. We estimate that the stellar density of RCP 32 would be more than 10 times lower than the cases of NGC 1052-DF2 and NGC 1052-DF4, with a difference in central surface brightness of approximately 3 mag arcsec<sup>-2</sup> lower. This is interesting since it would make similar observations in RCP 32 have a more reliable tip of the red giant branch distance estimate than for NGC 1052-DF2 and NGC 1052-DF4, at least a priori. All these arguments make RCP 32 an object of great interest and follow-up observations could have an impact on the discussion about the exotic properties of the LSBGs in this region.

*Acknowledgements.* We thank the anonymous referee for interesting suggestions that improved this work. We also thank Johan Knapen, Ignacio Trujillo and Mireia Montes for useful comments. The authors acknowledge financial support from the grants AYA2015-65973-C3-1-R and RTI2018-096228-B-C31 (MINECO/FEDER, UE), as well as from the State Agency for Research of the Spanish MCIU through the "Center of Excellence Severo Ochoa" award to the Instituto de Astrofísica de Andalucía (SEV-2017-0709). JR acknowledges support from the State Research Agency (AEI-MCINN) of the Spanish Ministry of Science and Innovation under the grant "The structure and evolution of galaxies and their central regions" with reference PID2019-105602GB-I00/10.13039/501100011033. JPG acknowledges funding support from Spanish public funds for research from project PID2019-107061GB-C63 from the "Programas Estatales de Generación de Conocimiento y Fortalecimiento Científico y Tecnológico del Sistema de I+D+i y de I+D+i Orientada a los Retos de la Sociedad". This project used data obtained with the Dark Energy Camera (DECam), which was constructed by the Dark Energy Survey (DES) collaboration. Funding for the DES Projects has been provided by the U.S. Department of Energy, the U.S. National Science Foundation, the Ministry of Science and Education of Spain, the Science and Technology Facilities Council of the United Kingdom, the Higher Education Funding Council for England, the National Center for Supercomputing Applications at the University of Illinois at Urbana-Champaign, the Kavli Institute of Cosmological Physics at the University of Chicago, Center for Cosmology and Astro-Particle Physics at the Ohio State University, the Mitchell Institute for Fundamental Physics and Astronomy at Texas A&M University, Financiadora de Estudos e Projetos, Fundacao Carlos Chagas Filho de Amparo, Financiadora de Estudos e Projetos, Fundacao Carlos Chagas Filho de Amparo a Pesquisa do Estado do Rio de Janeiro, Conselho Nacional de Desenvolvimento Científico e Tecnológico and the Ministerio da Ciencia, Tecnologia e Inovacao, the Deutsche Forschungsgemeinschaft and the Collaborating Institutions in the Dark Energy Survey. The Collaborating Institutions are Argonne National Laboratory, the University of California at Santa Cruz, the University of Cambridge, Centro de Investigaciones Energeticas, Medioambientales y Tecnológicas-Madrid, the University of Chicago, University College London, the DES-Brazil Consortium, the University of Edinburgh, the Eidgenössische Technische Hochschule (ETH) Zurich, Fermi National Accelerator Laboratory, the University of Illinois at Urbana-Champaign, the Institut de Ciències de l'Espai (IEEC/CSIC), the Institut de Física d'Altes Energies, Lawrence Berkeley National Laboratory, the Ludwig Maximilians Universität München and the associated Excellence Cluster Universe, the University of Michigan, NSF's NOIRLab, the University of Nottingham, the Ohio State University, the University of Pennsylvania, the University of Portsmouth, SLAC National Accelerator Laboratory, Stanford University, the University of Sussex, and Texas A&M University.

## References

- Abazajian, K. N., Adelman-McCarthy, J. K., Agüeros, M. A., et al. 2009, *ApJS*, 182, 543. doi:10.1088/0067-0049/182/2/543
- Abraham, R. G. & van Dokkum, P. G. 2014, *PASP*, 126, 55. doi:10.1086/674875

<sup>7</sup> We note here that Montes et al. (2021) have interpreted the elongation on the outskirts of NGC 1052-DF2 as a disk.



- Aihara, H., Arimoto, N., Armstrong, R., et al. 2018, PASJ, 70, S4. doi:10.1093/pasj/psx066
- Akhlaghi, M. & Ichikawa, T. 2015, ApJS, 220, 1. doi:10.1088/0067-0049/220/1/1
- Amorisco, N. C., Monachesi, A., Agnello, A., et al. 2018, MNRAS, 475, 4235. doi:10.1093/mnras/sty116
- Beasley, M. A., Romanowsky, A. J., Pota, V., et al. 2016, ApJ, 819, L20. doi:10.3847/2041-8205/819/2/L20
- Bertin, E., & Arnouts, S. 1996, A&AS, 117, 393
- Blakeslee, J. P. & Cantiello, M. 2018, Research Notes of the American Astronomical Society, 2, 146. doi:10.3847/2515-5172/aad90e
- Blanton, M. R., Lupton, R. H., Schlegel, D. J., et al. 2005, ApJ, 631, 208. doi:10.1086/431416
- Bournaud, F. & Duc, P.-A. 2006, A&A, 456, 481. doi:10.1051/0004-6361:20065248
- Bothun, G. D., Impey, C. D., Malin, D. F., et al. 1987, AJ, 94, 23. doi:10.1086/114443
- Bothun, G. D., Impey, C. D., & Malin, D. F. 1991, ApJ, 376, 404
- Bullock, J. S., Kolatt, T. S., Sigad, Y., et al. 2001, MNRAS, 321, 559. doi:10.1046/j.1365-8711.2001.04068.x
- Bullock, J. S. & Boylan-Kolchin, M. 2017, ARA&A, 55, 343. doi:10.1146/annurev-astro-091916-055313
- Burke, C. J., Aleo, P. D., Chen, Y.-C., et al. 2019, MNRAS, 490, 3952. doi:10.1093/mnras/stz2845
- Carlsten, S. G., Beaton, R. L., Greco, J. P., et al. 2019, ApJ, 879, 13. doi:10.3847/1538-4357/ab22c1
- Choque-Challapa, N., Aguerri, J. A. L., Mancera Piña, P. E., et al. 2021, MNRAS, 507, 6045. doi:10.1093/mnras/stab2420
- Cohen, Y., van Dokkum, P., Danieli, S., et al. 2018, ApJ, 868, 96. doi:10.3847/1538-4357/aae7c8
- Croft, R. A. C., Dalton, G. B., Efsthathiou, G., 1999, MNRAS, 305, 547. doi:10.1046/j.1365-8711.1999.02381.x
- Dalcanton, J. J., Spergel, D. N., Gunn, J. E., Schmidt, M., & Schneider, D. P. 1997, AJ, 114, 635
- Danieli, S., van Dokkum, P., Conroy, C., et al. 2019, ApJ, 874, L12. doi:10.3847/2041-8213/ab0e8c
- Danieli, S., van Dokkum, P., Abraham, R., et al. 2020, ApJ, 895, L4. doi:10.3847/2041-8213/ab8dc4
- Dark Energy Survey Collaboration, Abbott, T., Abdalla, F. B., et al. 2016, MNRAS, 460, 1270. doi:10.1093/mnras/stw641
- de Blok, W. J. G., McGaugh, S. S., Bosma, A., et al. 2001, ApJ, 552, L23. doi:10.1086/320262
- Dey, A., Schlegel, D. J., Lang, D., et al. 2019, AJ, 157, 168. doi:10.3847/1538-3881/ab089d
- Duc, P.-A. 2012, Astrophysics and Space Science Proceedings, 28, 305. doi:10.1007/978-3-642-22018-0\_37
- Emsellem, E., van der Burg, R. F. J., Fensch, J., et al. 2019, A&A, 625, A76. doi:10.1051/0004-6361/201834909
- Erwin, P. 2015, ApJ, 799, 226. doi:10.1088/0004-637X/799/2/226
- Famaey, B., McGaugh, S., & Milgrom, M. 2018, MNRAS, 480, 473. doi:10.1093/mnras/sty1884
- Fensch, J., van der Burg, R. F. J., Jeřábková, T., et al. 2019, A&A, 625, A77. doi:10.1051/0004-6361/201834911
- Ferguson, H. C., & Sandage, A. 1988, AJ, 96, 1520
- Fliri, J. & Trujillo, I. 2016, MNRAS, 456, 1359. doi:10.1093/mnras/stv2686
- Forbes, D. A. 2017, MNRAS, 472, L104. doi:10.1093/mnras/lsx148
- Forbes, D. A., Alabi, A., Brodie, J. P., et al. 2019, MNRAS, 489, 3665. doi:10.1093/mnras/stz2420
- Geller, M. J., Diaferio, A., Kurtz, M. J., et al. 2012, AJ, 143, 102. doi:10.1088/0004-6256/143/4/102
- Greco, J. P., Greene, J. E., Strauss, M. A., et al. 2018, ApJ, 857, 104. doi:10.3847/1538-4357/aab842
- Greco, J. P., van Dokkum, P., Danieli, S., et al. 2021, ApJ, 908, 24. doi:10.3847/1538-4357/abd030
- Haigh, C., Chamba, N., Venhola, A., et al. 2021, A&A, 645, A107. doi:10.1051/0004-6361/201936561
- Haslbauer, M., Banik, I., Kroupa, P., et al. 2019, MNRAS, 489, 2634. doi:10.1093/mnras/stz2270
- Hearin, A. P., Campbell, D., Tollerud, E., Behroozi, P., Diemer, B., Goldbaum, N. J., Jennings, E., et al., 2017, AJ, 154, 190. doi:10.3847/1538-3881/aa859f
- Honscheid, K. & DePoy, D. L. 2008, arXiv:0810.3600
- Impey, C., Bothun, G., & Malin, D. 1988, ApJ, 330, 634
- Infante-Sainz, R., Trujillo, I., & Román, J. 2020, MNRAS, 491, 5317. doi:10.1093/mnras/stz3111
- Janz, J., Laurikainen, E., Laine, J., et al. 2016, MNRAS, 461, L82. doi:10.1093/mnras/slw104
- Jordán, A., McLaughlin, D. E., Côté, P., et al. 2007, ApJS, 171, 101. doi:10.1086/516840
- Kadowaki, J., Zaritsky, D., Donnerstein, R. L., et al. 2021, arXiv:2110.00015
- Karachentsev, I. D., Karachentseva, V. E., Suchkov, A. A., et al. 2000, A&AS, 145, 415. doi:10.1051/aas:2000249
- Kazantzidis, S., Lokas, E. L., Callegari, S., et al. 2011, ApJ, 726, 98. doi:10.1088/0004-637X/726/2/98
- Keim, M. A., van Dokkum, P., Danieli, S., et al. 2021, arXiv:2109.09778
- Kennicutt, R. C. 1989, ApJ, 344, 685. doi:10.1086/167834
- Klypin, A., Kravtsov, A. V., Valenzuela, O., et al. 1999, ApJ, 522, 82. doi:10.1086/307643
- Koda, J., Yagi, M., Yamanoi, H., et al. 2015, ApJ, 807, L2. doi:10.1088/2041-8205/807/1/L2
- Kroupa, P., Haghi, H., Javanmardi, B., et al. 2018, Nature, 561, E4. doi:10.1038/s41586-018-0429-z
- Landy, S. D. & Szalay, A. S. 1993, ApJ, 412, 64. doi:10.1086/172900
- Laureijs, R., Amiaux, J., Arduini, S., et al. 2011, arXiv:1110.3193
- Lee, J., Shin, E.-jin, & Kim, J.-hoon. 2021, ApJ, 917, L15. doi:10.3847/2041-8213/ac16e0
- Lewis, G. F., Brewer, B. J., & Wan, Z. 2020, MNRAS, 491, L1. doi:10.1093/mnras/slz157
- LSST Science Collaboration, Abell, P. A., Allison, J., et al. 2009, arXiv:0912.0201
- Mancera Piña, P. E., Aguerri, J. A. L., Peletier, R. F., et al. 2019, MNRAS, 485, 1036. doi:10.1093/mnras/stz238
- Martin, N. F., Collins, M. L. M., Longeard, N., et al. 2018, ApJ, 859, L5. doi:10.3847/2041-8213/aac216
- Martin, G., Kaviraj, S., Laigle, C., et al. 2019, MNRAS, 485, 796. doi:10.1093/mnras/stz356
- Martínez-Delgado, D., Makarov, D., Javanmardi, B., et al. 2021, A&A, 652, A48. doi:10.1051/0004-6361/202141242
- Martínez-Delgado, D., Cooper, A. P., Roman, J., et al. 2021, arXiv:2104.06071
- Merritt, A., van Dokkum, P., Danieli, S., et al. 2016, ApJ, 833, 168. doi:10.3847/1538-4357/833/2/168
- Mihos, J. C., Carr, C. T., Watkins, A. E., et al. 2018, ApJ, 863, L7. doi:10.3847/2041-8213/aad62e
- Monelli, M. & Trujillo, I. 2019, ApJ, 880, L11. doi:10.3847/2041-8213/ab2fd2
- Montes, M., Infante-Sainz, R., Madrigal-Aguado, A., et al. 2020, ApJ, 904, 114. doi:10.3847/1538-4357/abc340
- Montes, M., Trujillo, I., Infante-Sainz, R., et al. 2021, ApJ, 919, 56. doi:10.3847/1538-4357/ac0d55
- Moore, B., Ghigna, S., Governato, F., et al. 1999, ApJ, 524, L19. doi:10.1086/312287
- Müller, O., Jerjen, H., & Binggeli, B. 2017, A&A, 597, A7. doi:10.1051/0004-6361/201628921
- Müller, O., Rich, R. M., Román, J., et al. 2019, A&A, 624, L6. doi:10.1051/0004-6361/201935463
- Nusser, A. 2019, MNRAS, 484, 510. doi:10.1093/mnras/sty3532
- Ogiya, G. 2018, MNRAS, 480, L106. doi:10.1093/mnras/sly138
- Patuel, G., Petit, C., Prugniel, P., et al. 2003, A&A, 412, 45. doi:10.1051/0004-6361:20031411
- Peng, C. Y., Ho, L. C., Impey, C. D., et al. 2010, AJ, 139, 2097. doi:10.1088/0004-6256/139/6/2097
- Pierce, M., Brodie, J. P., Forbes, D. A., et al. 2005, MNRAS, 358, 419. doi:10.1111/j.1365-2966.2005.08778.x
- Prole, D. J., Davies, J. I., Keenan, O. C., et al. 2018, MNRAS, 478, 667. doi:10.1093/mnras/sty1021
- Prole, D. J., van der Burg, R. F. J., Hilker, M., et al. 2019, MNRAS, 488, 2143. doi:10.1093/mnras/stz1843
- Prole, D. J., Hilker, M., van der Burg, R. F. J., et al. 2019, MNRAS, 484, 4865. doi:10.1093/mnras/stz326
- Prole, D. J., van der Burg, R. F. J., Hilker, M., et al. 2021, MNRAS, 500, 2049. doi:10.1093/mnras/staa3296
- Rejkuba, M. 2012, Ap&SS, 341, 195. doi:10.1007/s10509-012-0986-9
- Román, J. & Trujillo, I. 2017, MNRAS, 468, 703. doi:10.1093/mnras/stx438
- Román, J. & Trujillo, I. 2017, MNRAS, 468, 4039. doi:10.1093/mnras/stx694
- Román, J. & Trujillo, I. 2018, Research Notes of the American Astronomical Society, 2, 144. doi:10.3847/2515-5172/aad8b8
- Román, J., Beasley, M. A., Ruiz-Lara, T., et al. 2019, MNRAS, 486, 823. doi:10.1093/mnras/stz835
- Román, J., Trujillo, I., & Montes, M. 2020, A&A, 644, A42. doi:10.1051/0004-6361/201936111
- Román, J., Jones, M. G., Montes, M., et al. 2021, A&A, 649, L14. doi:10.1051/0004-6361/202141001
- Ruiz-Lara, T., Trujillo, I., Beasley, M. A., et al. 2019, MNRAS, 486, 5670. doi:10.1093/mnras/stz1237
- Saifollahi, T., Trujillo, I., Beasley, M. A., et al. 2021, MNRAS, 502, 5921. doi:10.1093/mnras/staa3016
- Sales, L. V., Navarro, J. F., Peñafiel, L., et al. 2020, MNRAS, 494, 1848. doi:10.1093/mnras/staa854
- Sandage, A., & Binggeli, B. 1984, AJ, 89, 919
- Schlafly, E. F., & Finkbeiner, D. P. 2011, ApJ, 737, 103

- Sérsic, J. L. 1968, Cordoba, Argentina: Observatorio Astronomico, 1968
- Shen, Z., van Dokkum, P., & Danieli, S. 2021, *ApJ*, 909, 179. doi:10.3847/1538-4357/abdd29
- Shen, Z., Danieli, S., van Dokkum, P., et al. 2021, *ApJ*, 914, L12. doi:10.3847/2041-8213/ac0335
- Spergel, D., Gehrels, N., Baltay, C., et al. 2015, arXiv:1503.03757
- Tanoglidis, D., Čiprijanović, A., & Drlica-Wagner, A. 2021, *Astronomy and Computing*, 35, 100469. doi:10.1016/j.ascom.2021.100469
- Tanoglidis, D., Drlica-Wagner, A., Wei, K., et al. 2021, *ApJS*, 252, 18. doi:10.3847/1538-4365/abca89
- Theureau, G., Hanski, M. O., Coudreau, N., et al. 2007, *A&A*, 465, 71. doi:10.1051/0004-6361:20066187
- Trujillo, I., Beasley, M. A., Borlaff, A., et al. 2019, *MNRAS*, 486, 1192. doi:10.1093/mnras/stz771
- Trujillo, I., D’Onofrio, M., Zaritsky, D., et al. 2021, *A&A*, 654, A40. doi:10.1051/0004-6361/202141603
- Trujillo-Gomez, S., Kruijssen, J. M. D., & Reina-Campos, M. 2021, arXiv:2103.08610
- Trujillo-Gomez, S., Kruijssen, J. M. D., Keller, B. W., et al. 2021, *MNRAS*, 506, 4841. doi:10.1093/mnras/stab1895
- Tuccillo, D., Huertas-Company, M., Decencièrre, E., et al. 2018, *MNRAS*, 475, 894. doi:10.1093/mnras/stx3186
- Tully, R. B., Courtois, H. M., Dolphin, A. E., et al. 2013, *AJ*, 146, 86. doi:10.1088/0004-6256/146/4/86
- van Dokkum, P. G., Abraham, R., Merritt, A., et al. 2015, *ApJ*, 798, L45. doi:10.1088/2041-8205/798/2/L45
- van Dokkum, P., Danieli, S., Cohen, Y., et al. 2018, *Nature*, 555, 629. doi:10.1038/nature25767
- van Dokkum, P., Danieli, S., Cohen, Y., et al. 2018, *ApJ*, 864, L18. doi:10.3847/2041-8213/aada4d
- van Dokkum, P., Cohen, Y., Danieli, S., et al. 2018, *ApJ*, 856, L30. doi:10.3847/2041-8213/aab60b
- van Dokkum, P., Danieli, S., Abraham, R., et al. 2019, *ApJ*, 874, L5. doi:10.3847/2041-8213/ab0d92
- van Dokkum, P., Danieli, S., Romanowsky, A., et al. 2019, *Research Notes of the American Astronomical Society*, 3, 29. doi:10.3847/2515-5172/ab05d6
- Venhola, A., Peletier, R., Laurikainen, E., et al. 2017, *A&A*, 608, A142. doi:10.1051/0004-6361/201730696
- Venhola, A., Peletier, R., Laurikainen, E., et al. 2019, *A&A*, 625, A143. doi:10.1051/0004-6361/201935231
- Villegas, D., Jordán, A., Peng, E. W., et al. 2010, *ApJ*, 717, 603. doi:10.1088/0004-637X/717/2/603
- Weinmann, S. M., van den Bosch, F. C., Yang, X., et al. 2006, *MNRAS*, 366, 2. doi:10.1111/j.1365-2966.2005.09865.x
- Whiting, A. B., Hau, G. K. T., Irwin, M., et al. 2007, *AJ*, 133, 715. doi:10.1086/510309
- Zaritsky, D., Donnerstein, R., Dey, A., et al. 2019, *ApJS*, 240, 1. doi:10.3847/1538-4365/aaefe9
- Zonoozi, A. H., Haghi, H., & Kroupa, P. 2021, *MNRAS*, 504, 1668. doi:10.1093/mnras/stab789

**Table A.1.** Spectroscopically confirmed galaxies in  $0.003 < z < 0.008$ .

| Name                      | R.A.<br>deg | Dec.<br>deg | V rad<br>km s <sup>-1</sup> |
|---------------------------|-------------|-------------|-----------------------------|
| VV 525                    | 36.5887     | -9.84083    | 2109                        |
| MRK 1039                  | 36.8865     | -10.1656    | 2111                        |
| MRK 1042                  | 37.0190     | -10.1834    | 2133                        |
| DDO 023                   | 37.6061     | -10.7488    | 2102                        |
| SHOC 124                  | 37.9417     | -9.14658    | 1608                        |
| [KKS2000] 51              | 38.4877     | -6.36005    | 1410                        |
| NGC 0988                  | 38.8656     | -9.35619    | 1510                        |
| NGC 0991                  | 38.8862     | -7.15443    | 1532                        |
| NGC 1022                  | 39.6363     | -6.67743    | 1453                        |
| LEDA 4014647              | 39.7021     | -8.04937    | 1665                        |
| NGC 1035                  | 39.8712     | -8.13294    | 1241                        |
| NGC 1042                  | 40.0999     | -8.43354    | 1371                        |
| UGCA 038                  | 40.1258     | -6.10639    | 1325                        |
| NGC 1047                  | 40.1368     | -8.14767    | 1340                        |
| NGC 0961                  | 40.2604     | -6.93592    | 1295                        |
| NGC 1052                  | 40.2700     | -8.25576    | 1510                        |
| WISEA J024120.23-071705.9 | 40.3343     | -7.28500    | 1663                        |
| LEDA 1020521              | 40.3724     | -7.34611    | 1144                        |
| LEDA 1007217              | 40.3961     | -8.17348    | 1530                        |
| NGC 1052-DF2              | 40.4450     | -8.40333    | 1803                        |
| WISEA J024149.89-075530.4 | 40.4581     | -7.92502    | 1372                        |
| WISEA J024246.88-073231.2 | 40.6953     | -7.54210    | 1344                        |
| MCG -01-08-001            | 40.9283     | -6.65139    | 1410                        |
| NGC 1084                  | 41.4996     | -7.57847    | 1407                        |
| [SB2012] 023              | 42.0664     | -8.28792    | 1375                        |
| WISEA J024839.94-074848.2 | 42.1665     | -7.81342    | 1465                        |
| NGC 1110                  | 42.2899     | -7.83754    | 1333                        |
| LEDA 1003250              | 42.2966     | -8.47465    | 1430                        |
| WISEA J024913.38-080651.3 | 42.3059     | -8.11505    | 1447                        |
| LEDA 4016901              | 43.3694     | -8.98488    | 1425                        |
| LEDA 976989               | 43.3897     | -10.5357    | 1507                        |
| NGC 1140                  | 43.6399     | -10.0278    | 1501                        |
| LEDA 3994671              | 43.8319     | -10.8213    | 1572                        |
| IC 0271                   | 43.9977     | -12.0078    | 1607                        |

## Appendix A: Spectroscopically confirmed galaxies in $0.003 < z < 0.008$